





RESEARCH ARTICLE

Inorganic phosphate exporter heterozygosity in mice leads to brain vascular calcification, microangiopathy, and microgliosis

Upasana Maheshwari¹  | José M. Mateos² | Ulrike Weber-Stadlbauer^{3,4} | Ruiqing Ni^{4,5}  | Virgil Tamatey^{6,7}  | Sucheta Sridhar^{1,4} | Alejandro Restrepo¹ | Pim A. de Jong⁸ | Sheng-Fu Huang¹ | Johanna Schaffenrath¹ | Sebastian A. Stifter⁹ | Flora Szeri⁶ | Melanie Greter⁹ | Huiberdina L. Koek¹⁰ | Annika Keller^{1,4} 

¹Department of Neurosurgery, Clinical Neuroscience Center, University Hospital Zurich, University of Zurich, Zurich, Switzerland

²Center for Microscopy and Image analysis, University of Zurich, Zurich, Switzerland

³Institute of Veterinary Pharmacology and Toxicology, University of Zurich-Vetsuisse, University of Zurich, Zurich, Switzerland

⁴Neuroscience Center Zurich, University of Zurich and ETH Zurich, Zurich, Switzerland

⁵Institute for Biomedical Engineering, University of Zurich and ETH Zurich, Zurich, Switzerland

⁶Research Centre for Natural Sciences, Institute of Enzymology, Budapest, Hungary

⁷Doctoral School of Biology, ELTE Eotvos Lorand University, Budapest, Hungary

⁸Department of Radiology, University Medical Center Utrecht, Utrecht University, Utrecht, The Netherlands

⁹Institute of Experimental Immunology, University of Zurich, Zurich, Switzerland

¹⁰Department of Geriatric Medicine, University Medical Centre Utrecht, Utrecht University, Utrecht, The Netherlands

Abstract

Calcification of the cerebral microvessels in the basal ganglia in the absence of systemic calcium and phosphate imbalance is a hallmark of primary familial brain calcification (PFBC), a rare neurodegenerative disorder. Mutation in genes encoding for sodium-dependent phosphate transporter 2 (SLC20A2), xenotropic and polytropic retrovirus receptor 1 (XPR1), platelet-derived growth factor B (PDGFB), platelet-derived growth factor receptor beta (PDGFRB), myogenesis regulating glycosidase (MYORG), and junctional adhesion molecule 2 (JAM2) are known to cause PFBC. Loss-of-function mutations in *XPR1*, the only known inorganic phosphate exporter in metazoans, causing dominantly inherited PFBC was first reported in 2015 but until now no studies in the brain have addressed whether loss of one functional allele leads to pathological alterations in mice, a commonly used organism to model human diseases. Here we show that mice heterozygous for *Xpr1* (*Xpr1*^{WTlacZ}) present with reduced inorganic phosphate levels in the cerebrospinal fluid and age- and sex-dependent growth of vascular calcifications in the thalamus. Vascular calcifications are surrounded by vascular basement membrane and are located at arterioles in the smooth muscle layer. Similar to previously characterized PFBC mouse models, vascular calcifications in *Xpr1*^{WTlacZ} mice contain bone matrix proteins and are surrounded by reactive astrocytes and microglia. However, microglial activation is not confined to calcified vessels but shows a widespread presence. In addition to vascular calcifications, we observed vessel

Abbreviations: AB, alcian blue; ALP, alkaline phosphatase; APP, amyloid precursor protein; AR, alizarin red; ASMA, alpha smooth muscle actin; AT-SEM, array tomography-scanning electron microscope; BBB, blood-brain barrier; BM, basement membrane; BSA, bovine serum albumin; CD31, cluster of differentiation 31; CLEC7A, C-type lectin domain family 7 member A; CSF, cerebrospinal fluid; CT, computed tomography; DAB, 3,3'-diaminobenzidine; DAPI, 4',6-diaminodino-2-phenylindole; GFAP, glial fibrillary acidic protein; HE, hematoxylin and eosin; IBA1, ionized calcium-binding adapter molecule 1; ICAM-1, intercellular adhesion molecule 1; iDISCO, immunolabeling-enabled three-dimensional imaging of solvent-cleared organs; iPSC, induced pluripotent stem cell; IRES, internal ribosome entry site; JAM2, junctional adhesion molecule; LAMA1, laminin subunit alpha 1; LOF, loss-of-function; MRI, magnetic resonance imaging; MYORG, myogenesis regulating glycosidase; PAS, periodic acid-Schiff; PBS, phosphate-buffered saline; PDGFB, platelet-derived growth factor subunit B; PDGFRB, platelet-derived growth factor receptor beta; PFA, paraformaldehyde; PFBC, primary familial brain calcification; Pi, inorganic phosphate; PPI, pre-pulse inhibition; SLC20A2, solute carrier family 20 member 2; SVZ, sub-ventricular zone; SWI, susceptibility-weighted imaging; TEM, transmission electron microscopy; VK, von Kossa; VSMC, vascular smooth muscle cell; WT, wild type; X-GAL, 5-bromo-4-chloro-3-indolyl β-D-galactopyranoside; X-MLV, xenotropic murine leukemia viruses; XPR1, xenotropic polytropic retrovirus receptor 1.

[Correction added on 11 August 2023, after first online publication: Flora Szeri's affiliation has been corrected.]

This is an open access article under the terms of the [Creative Commons Attribution-NonCommercial-NoDerivs](https://creativecommons.org/licenses/by-nc-nd/4.0/) License, which permits use and distribution in any medium, provided the original work is properly cited, the use is non-commercial and no modifications or adaptations are made.

© 2023 The Authors. *Brain Pathology* published by John Wiley & Sons Ltd on behalf of International Society of Neuropathology.

Correspondence

Annika Keller and Upasana Maheshwari,
Department of Neurosurgery, Clinical
Neuroscience Center, University Hospital
Zurich, University of Zurich, Zurich,
Switzerland.

Emails: annika.keller@usz.ch and
upasana.maheshwari@usz.ch

Funding information

National Research Development and
Innovation Office, Grant/Award Number:
FK131946; New National Excellence Program
of the Ministry for Innovation and Technology
from the source of the NKFIH, Grant/Award
Number: UNKP-22-5-SE-2; Novartis
FreeNovation; Schweizerische Multiple
Sklerose Gesellschaft; Schweizerischer
Nationalfonds zur Förderung der
Wissenschaftlichen Forschung, Grant/Award
Number: 310030_188952; Stiftung Synapsis -
Alzheimer Forschung Schweiz AFS,
Grant/Award Number: 2019-P102; The
Hungarian Academy of Sciences, Grant/Award
Number: BO/00730/19/8

tortuosity and transmission electron microscopy analysis revealed microangiopathy—endothelial swelling, phenotypic alterations in vascular smooth muscle cells, and thickening of the basement membrane.

KEYWORDS

acoustic startle response, dark microglia, inflammation, retina, scanning electron microscopy, sexual dimorphism

1 | INTRODUCTION

Xenotropic and polytropic retrovirus receptor 1 (XPR1) was initially identified as a cell surface receptor for polytropic and xenotropic murine leukemia virus (X-MLVs) [1, 2]. XPR1 is a multipass membrane protein containing a cytosolic amino-terminal SPX domain (name derived from suppressor of yeast *gal* (SYG1), yeast phosphatase 81 (Pho81), and human XPR1), and is the only known inorganic phosphate (Pi) exporter in metazoans [3]. Eukaryotic SPX domain containing proteins have been identified as key players in maintaining cellular phosphate homeostasis by sensing the intracellular Pi concentration. These proteins bind to inositol polyphosphates, concentrations of which change in response to cellular Pi level and thereby contribute to intracellular phosphate homeostasis [4]. Accordingly, XPR1-mediated Pi efflux is regulated by inositol pyrophosphates [5–7].

There is emerging evidence for the role of XPR1 in progression of various carcinomas due to its increased expression or activity [8–11]. On the other hand, loss-of-function (LOF) mutations in *XPR1* (OMIM no. 616413) are causal of autosomal dominantly inherited neuropsychiatric disorder named primary familial brain calcification (PFBC) [12]. Histologically, the most striking feature of PFBC is the presence of vascular calcifications in the basal ganglia [13], which cover vessels like “pearls on a string.” While the clinical penetrance of PFBC is incomplete, radiological penetrance is 100% by the age of 50 [14]. The affected brain regions may also include thalamus, cortical white and grey matter, cerebellum, and brain stem [15].

PFBC is clinically heterogeneous and patients could present with cognitive decline, movement disorders, and psychiatric alterations [16]. In addition to *XPR1*, mutations

in *SLC20A2* (OMIM no. 213600), *PDGFRB* (OMIM no. 615007), and *PDGFB* (OMIM no. 615483) cause autosomal dominant PFBC [17–19]. Biallelic mutations in *MYORG* (OMIM no. 618317) and *JAM2* (OMIM no. 618824) cause autosomal recessive PFBC [20, 21]. Missense mutations in *XPR1* lead to impaired cell surface expression and phosphate efflux, suggesting altered XPR1-mediated phosphate export as a pathogenic mechanism [12, 22–24]. A few autopsy studies and case reports of patients with PFBC provide evidence of vascular insufficiency and compromised blood–brain barrier (BBB) [25–27]. Neuronal loss has been reported in severely calcified areas, but neurons generally remain preserved in PFBC [28, 29]. There is considerable heterogeneity in the histopathological findings of PFBC, and it is unclear to what extent different histopathological and neurological features are causally related [29–31].

The pathophysiology of PFBC is poorly understood, and it is not known how functionally different PFBC genes (e.g., inorganic phosphate importer [SLC20A2] and exporter [XPR1], and a growth factor [PDGFB] and its receptor [PDGFRB]) lead to a common histopathological phenotype (i.e., calcification of blood vessels) and disease. Several cell types in the brain express these proteins and therefore the disease-causing mutations could potentially affect their function. This in turn could lead to the formation of vessel-associated calcifications and neuronal dysfunction and thus, the pathogenesis of PFBC is likely multifactorial. Also, although different mouse models of PFBC (i.e., knockouts of *Slc20a2*, *Myorg*, *Jam2*), and PDGFB hypomorph (*Pdgfb^{ret/ret}*, retention motif knockout) mimic the characteristic histopathological feature of PFBC; the formation of vascular calcifications, they nevertheless show differences in histopathology and behavioral changes [19–21, 32, 33]. Currently, no studies have

reported the consequences of LOF of *XPR1* in mouse brain. In mice, homozygous knockout of *Xpr1* is perinatal lethal and, both, full knockout and heterozygosity of *Xpr1* leads to placental calcification [34, 35]. In this study, we report that loss of one functional *Xpr1* allele leads to reduction in Pi levels in the cerebrospinal fluid (CSF) and brain vascular calcification in adult mice. We show that in *Xpr1* heterozygous mice, brain vascular calcifications develop in the thalamus starting at the age of 7 months. Growth of calcifications is sex-dependent, with an increased calcification load in males. Calcifications appear inside the vascular smooth muscle coat of thalamic arterioles and are surrounded by activated microglia and reactive astrocytes. *Xpr1* heterozygous mice present with microangiopathy and narrowed lumen of arterioles, a pathology that has so far not been described in other mouse models of PFBC. In addition, we describe widespread presence of activated microglia in *Xpr1* heterozygous mice, both around calcifications and in other regions, based on their morphology, marker expression, and their ultrastructural appearance under the electron microscopy.

2 | MATERIALS AND METHODS

2.1 | Mice

Xpr1 heterozygous mice (C57BL/6N-*Xpr1*^{tm1a(KOMP)Wsi}/MbpMmucd, MGI: 4362650; referred to as *Xpr1*^{WT/lacZ} in this manuscript), generated by promoter-driven knockout first allele strategy, were obtained from KOMP repository, UC Davis [36]. The information about site of targeted insertion in this mouse line is available at MGI database. The mice were housed under 12-h light/dark cycle in individually ventilated cages and were given food and water ad libitum. *Xpr1* heterozygous males were bred with C57BL/6NCrl females to obtain mice for experimentation. Mice of both sexes were used for experiments. Genotyping biopsies were collected at the time of weaning. Genotyping was done according to the KOMP PCR design protocol ID 41632. The age of mice used for experiments was 7–16 months. Experiments were carried out in accordance with the protocols approved by the cantonal veterinary office Zurich under permit numbers ZH151/2017 and ZH194/2020. Animal research was done according to ARRIVE guidelines 2.0.

2.2 | Quantitative PCR

RNA was isolated from snap frozen tissue (cortex, deep brain, cerebellum, liver, lung, and kidney) using RNeasy Plus kit (Qiagen no. 74134) following manufacturer's instruction. A total of 250 ng of isolated RNA was reverse transcribed to cDNA using GoScript Reverse

Transcription System (Promega no. A5000) following manufacturer's protocol. Transcript levels were assessed by quantitative PCR (qPCR) using PowerUp SYBR green master mix (Applied Biosystems no. A25742) in Applied Biosystems 7500 real-time PCR system. The mRNA levels of *Xpr1* were normalized to mRNA levels of *Gapdh*. Tissues from three *Xpr1*^{WT/WT} and four *Xpr1*^{WT/lacZ} mice were analyzed. Primers used for qPCR were as follows: *Gapdh* forward primer: 5'-GACTTCAACAGCAACTCCCAC-3'; *Gapdh* reverse primer: 5'-TCCACCACCTGTTGCTGTA-3'; *Xpr1* forward primer: 5'-ATCGCTGGATGTGCAGAAAGA-3'; *Xpr1* reverse primer: 5'-CCTATGTTGGACACGCTCCT-3'.

2.3 | Antibodies

Primary antibodies used for immunofluorescence staining are listed in Table S2. Fluorescently (Alexa Fluor 488, Cy3, Alexa Fluor 647) labeled secondary antibodies suitable for multiple labeling made in donkey were purchased from Jackson ImmunoResearch. Secondary antibodies were used in 1:600 dilution. All sections were counter stained with 4',6-diamidino-2-phenylindole dihydrochloride (DAPI; Sigma-Aldrich, cat. no. D9542, stock concentration 10 mg/mL, 1:10,000) in PBS.

2.4 | Immunofluorescent staining on mouse retina and brain vibratome slices

Mice were deeply anaesthetized with ketamine–xylazine cocktail and transcardially perfused with ice-cold PBS followed by ice-cold 4% paraformaldehyde (PFA) in PBS, pH 7.2. The brain and eyes were removed and post-fixed for 6 h in 4% PFA in PBS at 4°C with shaking. Brains were sectioned with a vibratome (Leica VT1000S) into 60- μ m thick slices and stored in 24 well plate in 0.01% NaN₃ in PBS. Retina was dissected from fixed eyes before proceeding with immunofluorescent staining. For co-staining with anti-LAMA1 antibody, *Xpr1*^{WT/lacZ} mice were deeply anesthetized with ketamine–xylazine cocktail and transcardially perfused with ice-cold PBS. The brains were hemispherized, snap-frozen in liquid nitrogen, and stored at –80°C until used. For sectioning, the brains were thawed in 4% PFA in PBS at 4°C for 1 h and then sectioned with a vibratome into 100 μ m thick slices and stored in 24 well plate in 0.01% NaN₃ in PBS.

Retina or brain slices were blocked overnight in 1% bovine serum albumin (BSA), 0.1% Triton™ X-100 in PBS at 4°C. Followed by an incubation for 3 days at 4°C in primary antibody cocktail in 0.5% BSA and 0.05% Triton™ X-100 in PBS. Brain slices were washed four to five times with 0.5% BSA and 0.05% Triton™ X-100 in PBS at room temperature (RT). Slices were incubated

overnight at 4°C with secondary antibodies diluted in 0.5% BSA and 0.05% Triton™ X-100 in PBS. After this, slices were stained with DAPI, followed by washing in PBS for four to five times, and mounted in ProLong® Gold Antifade (Invitrogen). Immunohistochemistry stainings were imaged using a confocal laser scanning microscope (Leica SP8, objectives—×20 numerical aperture (NA): 0.7 or ×63 NA: 1.4). Images were analyzed with Fiji. For stains that exhibited a salt-and-pepper noise, a median filter of radius 0.2 was applied to remove the noise. For time course study, four to six *Xpr1^{WTlacZ}* mice per stage were analyzed. For all other immunofluorescence studies, a minimum of three animals of both genotypes were investigated per staining.

2.5 | Intravenous injection of dextran

Mice were acclimated to the restraining tube for 5 min. The tail vein injection of 1 mg 70 kDa-dextran conjugated to Texas Red (10 mg/mL stock, D1864, Invitrogen) was performed using the insulin syringe. Thirty seconds after injection the animal was euthanized with CO₂ method and the brain was dissected out. Dissected brains were post-fixed in 4% PFA in PBS with shaking for 6 h at 4°C. Post fixation, brains were stored in 0.01% NaN₃ in PBS until used for immunohistochemistry and imaging. Four *Xpr1^{WTlacZ}* mice were analyzed.

2.6 | Histochemistry and immunohistochemistry

Mice were deeply anaesthetized with ketamine–xylazine cocktail and transcardially perfused with ice-cold PBS followed by ice-cold 4% PFA in PBS, pH 7.2. Brains were dissected and embedded in paraffin. Tissue sections (2 µm) were stained for hematoxylin and eosin, periodic acid-Schiff stain, and alcian blue using standard protocols. Von-Kossa staining was done using von-Kossa Silver Staining Kit (Sigma) as per the manufacturer's protocol. Microglia was detected using anti-IBA1 antibody (WAKO) on 2-µm paraffin sections. Sections were deparaffinized through graded alcohols and heat-induced antigen retrieval was performed in citrate buffer (0.01 M; pH 6.0). Sections were incubated with anti-IBA1 antibody (1 : 2500). Stainings were visualized using DAB (Sigma-Aldrich) and H₂O₂ (Sigma-Aldrich), after incubation with a biotinylated secondary antibody (Vector Laboratories) followed by the ABC complex solution (Vector laboratories). Sections were counterstained with hematoxylin. Stained paraffin sections were imaged with Zeiss Axio Scan.Z1 (objectives—×10 [NA: 0.45] and ×40 air [NA: 0.95]). Images were visualized and analyzed with ZEN image analysis module. Five *Xpr1^{WT/WT}* and seven *Xpr1^{WTlacZ}* mice were analyzed.

2.7 | Whole brain immunostaining, clearing, and imaging

Whole brain staining and clearing was done according to iDISCO+ protocol with minor modifications in the antibody incubation time [37]. Hemispherized brains from 16-month-old mice were incubated with primary antibody (goat anti-osteopontin, 1:500) for 3 weeks at 37°C with rotation and with secondary antibody (donkey anti-goat Alexa Fluor 488, 1:1000) for 1 week at 37°C with rotation. Whole brain imaging was done using an in-house built light sheet microscope *mesoSPIM* [38]. Stained and cleared hemispherized brains were imaged with ×1 and ×6.3 zoom. Images were analyzed using Fiji- ImageJ and visualized using Bitplane—Imaris software. Technical details of *mesoSPIM* microscope are described elsewhere (www.mesos pim.org). Three *Xpr1^{WTlacZ}* female, four *Xpr1^{WTlacZ}* male and two *Xpr1^{WT/WT}* male mice were analyzed.

2.8 | Transmission and scanning electron microscopy

Mice were transcardially perfused under anesthesia (ketamine–xylazine cocktail) with ice-cold PBS followed by freshly made Karnovsky's fixative—2% PFA (Polysciences, no. 18814-10), 2.5% glutaraldehyde (Polysciences, no. 01909-10) in 0.1 M cacodylate buffer (pH 7.4) (Polyscience, no. 18661-500). Brains were dissected and 1 mm thick coronal sections were cut with a brain matrix (World Precision Instruments, RBMA-200C). Sections were kept in Karnovsky's fixative until sample preparation for EM. Coronal sections were washed in 0.1 M cacodylate buffer before incubation with 1% OsO₄ in 0.1 M cacodylate buffer for 1 h, and 1% aqueous uranyl acetate overnight. Samples were dehydrated in an ethanol series and embedded in Epon/Araldite (Sigma-Aldrich). Three *Xpr1^{WTlacZ}* and two *Xpr1^{WT/WT}* mice were analyzed.

2.8.1 | Transmission electron microscopy

Ultrathin (70 nm) sections were post-stained with lead citrate and examined with a Talos 120 transmission electron microscope at an acceleration voltage of 120 KV using a Ceta digital camera and the MAPS software package (Thermo Fisher Scientific).

2.8.2 | Array tomography scanning electron microscopy (AT-SEM)

The observed calcifications from TEM sections served as reference to identify the regions in the remaining block. We collected serial sections (100 nm) from these blocks on pieces of silicon wafer (10 mm × 20 mm) using an ARTOS 3D (Leica Microsystem) and an adapted holder [39].

Wafers were poststained with lead citrate and imaged with a scanning electron microscope (Apreo VS, ThermoFisher).

The array tomography workflow includes serial sections recognition, image region definition, autofunctions, and image acquisition [40]. Following imaging parameters were used: acceleration voltage: 1.18 keV, current: 0.1 nA, Optiplan modus, T1 detector, 4 mm working distance, and 3 μ s dwell time.

We used a python script to generate a position list of the XYZ coordinates for the tiff images which allowed us to load the tiff images into plugin TrakEM2 in Fiji [41, 42]. The alignment of the tiles was done with TrakEM2.

2.9 | Ex vivo susceptibility-weighted MRI (SWI-MRI) and phase imaging

Sixteen-month-old mice were deeply anesthetized using ketamine–xylazine cocktail and transcardially perfused with ice-cold PBS followed by ice-cold 4% PFA in PBS, pH 7.2. Brains were removed and post-fixed for 6 hours in 4% PFA at 4°C with shaking. Fixed brains were stored in 0.01% NaN₃ in PBS at 4°C until imaging. Ex vivo MRI was performed on a horizontal Bruker Biospec 9.4 T (Bruker Biospin GmbH) small animal MR system equipped with a cryogenic 2 × 2 radiofrequency surface coil probe (Bruker BioSpin AG). Dissected brains were placed in a 15 mL centrifuge tube filled with perfluoropolyether (Fomblin Y, LVAC 16/6, average molecular weight 2700, Sigma-Aldrich, USA), a proto-free compound that renders a dark background on MRI. Samples were measured at RT. A 3D gradient-recalled echo SWI sequence was recorded with the following parameters: field-of-view = 15 × 12 × 15 mm; image size = 248 × 200 × 36 mm, resulting in a spatial resolution of 60 × 60 × 417 μ m. One echo with an echo time = 12 ms; repetition time = 250 ms; flip angle = 15; number of averages = 4 within an acquisition scan time of 1 h, 59 min, and 24 s was recorded. A global and MAP-SHIM protocol with a field map (default setting) was used for shimming. SW and phase images were computed using the SWI processing module in ParaVision 6.0.1 (Bruker, Ettlingen, Germany) with the Gauss broadening = 1 mm and a mask weighting = 4. Three *Xpr1*^{WT/lacZ} female and four *Xpr1*^{WT/lacZ} male mice were analyzed.

2.9.1 | Quantification of calcifications on images generated using susceptibility-weighted imaging

Seven SWI datasets were analyzed. Serial images containing calcification-prone regions were selected for quantification. SWI images were compared with their phase image counterparts to ensure that the signal was due to a diamagnetic signal (i.e., presence of calcium). SWI

images were processed using Fiji (ImageJ), where images were contrast-enhanced, thresholded, and converted to a binary image [42]. The area covered by calcifications in a region of interest in one SWI image was calculated from the obtained binary images. The region of interest used on serial SWI slices remained constant across all analyzed datasets. Prism7 software (GraphPad) was used for statistical analysis (unpaired *t*-test).

2.10 | Measurement of calcium, phosphate, and alkaline phosphatase from plasma

A total of 200 to 300 μ L blood was drawn in via pre-heparinized 23G needle by cardiac puncture from deeply anesthetized (ketamine–xylazine cocktail) 9-month-old mice and placed in precooled Li-H300 tube. Blood was gently mixed with anticoagulants by inverting the tubes ×5 times. Tubes were centrifuged at 1000g for 10 min at 4°C and plasma was collected. All samples were aliquoted and then stored at –80°C until further use. The measurements were performed using AU480 Clinical Chemistry System (Beckman Coulter). Plasma concentration of calcium, inorganic phosphorous, and alkaline phosphatase was measured using Beckman Coulter Calcium Arsenazo (OSR60117), inorganic phosphorous (OSR6122), and alkaline phosphatase (OSR6004) kits, respectively, according to manufacturer's protocol. Statistical analyses (unpaired *t*-test) were done using Prism7 software (GraphPad). Nine *Xpr1*^{WT/WT} and eight *Xpr1*^{WT/lacZ} mice were analyzed.

2.11 | Measurement of phosphate from cerebrospinal fluid

One to five μ L of CSF was collected using capillaries from cisterna magna of deeply anesthetized mice (ketamine–xylazine cocktail). CSF was collected in a microtube and stored at –80°C until further use. Inorganic phosphate concentration of the CSF was determined with Malachite Green assay (MAK307, Merck Life Science) in 96 well flat-bottom microtiter plates, according to the manufacturer's instructions, with slight modifications. Briefly, 20 μ L Working reagent (100:1 Reagent A: Reagent B) containing malachite green and molybdate was added to a solution of 200 μ L containing 0.5 or 1 μ L of undiluted (singlets) or 5 μ L of ×10 diluted CSF samples (duplicates), depending on the available sample volume, or 40, 60 μ L of Pi standards (4–40 μ M Pi). The absorbance at 620 nm was determined in a kinetic manner at room temperature on an Enspire Multimode Plate reader (PerkinElmer). The difference in absorbance between samples and blank was calculated and quantified using the calibration standards at timepoints between 15 and 30 min showing linearity. Five *Xpr1*^{WT/WT} and four *Xpr1*^{WT/lacZ} mice were analyzed.

2.12 | Behavioral studies

Adult mice (7- to 8-month-old and 13- to 15-month-old) underwent behavioral testing in three cohorts. Younger animals underwent testing in one cohort that consisted of 23 mice ($n = 9$ *Xpr1*^{WT/lacZ} [four male and five female] and $n = 14$ *Xpr1*^{WT/WT} [six male and eight female] mice). Older animals were split into two cohorts (II and III) to obtain similar ages for behavioral testing, cohort II consisted of 16 mice ($n = 10$ *Xpr1*^{WT/lacZ} [six male and four female] and $n = 6$ *Xpr1*^{WT/WT} [two male and four female] mice) and cohort III consisted of 24 mice ($n = 15$ *Xpr1*^{WT/lacZ} [seven male and eight female] and $n = 9$ *Xpr1*^{WT/WT} [three male and six female] mice). Behavioral testing was carried out during the light phase in a dimly lit room. For all the tests, except prepulse inhibition, a digital camera was mounted above the maze. Images were captured at a rate of 5 Hz and transmitted to a PC running EthoVision tracking system (Noldus Information Technology, The Netherlands). The number of animals used for each test is given in the respective figure legends. Statistical analyses (unpaired *t*-test and two-way ANOVA) were done using Prism7 software (GraphPad). Outlier data from one *Xpr1*^{WT/lacZ} female and one *Xpr1*^{WT/WT} female was excluded from elevated plus maze and open field test, respectively.

2.12.1 | Elevated plus-maze

The elevated plus maze test was used to assess innate anxiety-like behavior. The apparatus was made of opaque acrylic glass and elevated at a height of 70 cm above floor level. It consisted of four equally spaced arms radiating out from a central square measuring 5 × 5 cm. Each arm was 30 cm long. Two opposing arms were enclosed by 15 cm high opaque walls from all sides except the side adjoining the central square. The other two arms were exposed, and the outer rim of the open arms was guarded by a perimeter border of 1 mm. The floor of the entire maze was covered by a grey plastic inlay that can be easily removed and cleansed with water between trials. The maze was located in a dimly lit experimental room. The light level in the open arms of the maze was balanced at 30 lux. A digital camera was mounted above the maze and images were transmitted at a rate of 5 Hz to a personal computer running the EthoVision (Noldus IT, Wageningen, The Netherlands) software allowing the tracking of the animal's position. To begin a trial, the mouse was placed in the center of the maze facing one of the open arms. It was allowed to move freely undisturbed for 5 min before being returned to the home cage.

Innate anxiety (IA) was indexed as a percent of time spent in the open arms during 5 min of exploration: IA = [(time spent in open arm/total exploration time)100].

2.12.2 | Prepulse inhibition

The set-up and analysis used were the same as described in Zarb et al. [43]. We assessed only females for this test as aged males were too heavy to fit into the PPI test chamber. Females above 50 g of weight were also excluded from the test. No significant difference in the weight of control and *Xpr1*^{WT/lacZ} female and male mice was observed (Figure S7I). However, males were significantly heavier than females (Figure S7J) and therefore not included in the PPI test.

Parameters and settings for open field test, spontaneous alternation test, and social interaction test were same as described in Zarb et al. [43].

3 | RESULTS

3.1 | *Xpr1* heterozygous mice develop calcifications in the thalamus

LOF mutations in *XPR1* are associated with an autosomal dominant form of PFBC in humans, presenting with bilateral vascular calcifications in the basal ganglia [12]. To investigate whether the absence of *Xpr1* would also lead to vascular calcification in the mice, we analyzed mice containing an IRES:*lacZ* trapping cassette inserted upstream of exon 2 (Figure S1a). Similar to *Xpr1*^{-/-} mice [35], *Xpr1*^{lacZ/lacZ} mice are neonatally lethal (Table S1), while *Xpr1*^{WT/lacZ} mice grow to adulthood. QPCR analysis showed that the expression of *Xpr1* mRNA is reduced in *Xpr1*^{WT/lacZ} tissue (Figure S1b). The expression of *lacZ*, as assessed by X-GAL staining, could only be seen in *Xpr1* heterozygous animals (named *Xpr1*^{WT/lacZ}, Figure S1c), thereby confirming the presence of a *lacZ* cassette. Based on the expression of *lacZ*, we show that *Xpr1* is ubiquitously expressed throughout the mouse brain (Figure S1c). For example, *Xpr1* is expressed in the hippocampus, in the cortical layers 2 and 5 (Figure S1c), in the subventricular zone (SVZ), and along blood vessels (Figure S1d). Histological analysis of 16-month-old *Xpr1*^{WT/lacZ} mice showed presence of nodules in the thalamus visible on paraffin sections stained with hematoxylin and eosin (HE), periodic acid-Schiff (PAS), and alcian blue (AB) (Figures 1A and S1e). These nodules were positive for stains used to detect calcium deposits—von Kossa (VK) and alizarin red (AR; Figure 1A). Smaller nodules visible by staining with HE, AB, PAS, and AR were also observed in brain tissue from 9-month-old *Xpr1*^{WT/lacZ} mice (Figure S1f), suggesting a progressive growth of calcification in these mice similar to reported studies in human cases and other mouse models of PFBC [19, 29, 44]. It is important to note that aged wild type mice have been reported to show calcification of thalamus [45–47]. However, in our study age-matched wild type controls seldom presented with

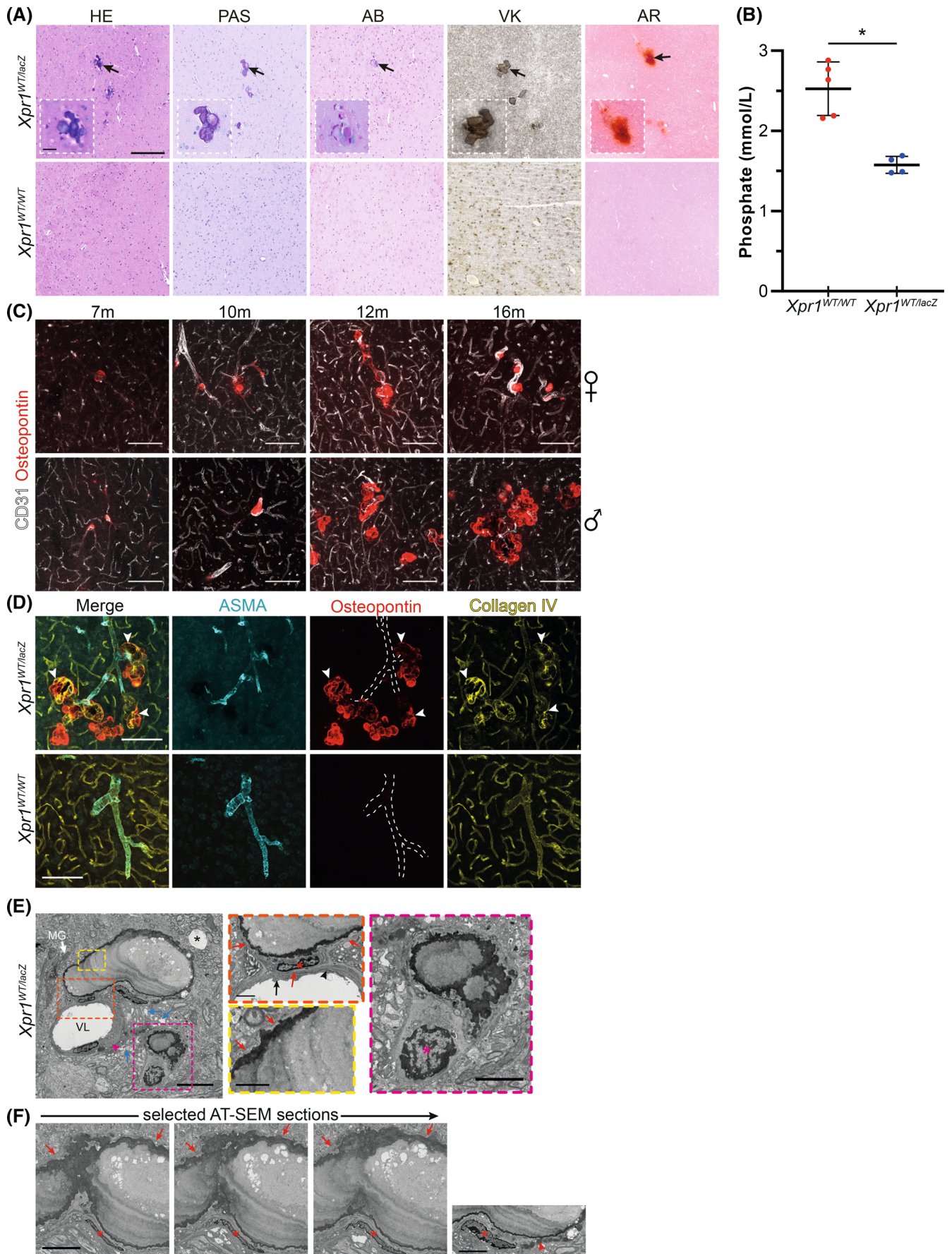


FIGURE 1 Legend on next page.

calcifications, whereas all 16-month-old *Xpr1*^{WT/lacZ} animals developed pronounced calcifications. This suggests that the pathology observed in the brains of *Xpr1*^{WT/lacZ} mice is caused by *Xpr1* heterozygosity and is not merely due to age.

In accordance with data from PFBC patients and mouse models [19, 33, 48], we did not detect changes in the plasma concentration of calcium (Figure S1g), Pi (Figure S1h), or alkaline phosphatase activity (Figure S1i) in *Xpr1*^{WT/lacZ} mice. However, reduced levels of Pi were identified in the cerebrospinal fluid (CSF) of *Xpr1*^{WT/lacZ} mice as compared with *Xpr1*^{WT/WT} mice (Figure 1B). Taken together, these data suggest the presence of brain calcifications in *Xpr1*^{WT/lacZ} mice similar to calcifications characterized in PFBC cases and mouse models.

3.2 | Arterioles are calcified in *Xpr1*^{WT/lacZ} mice

We next assessed whether the calcifications detected in *Xpr1*^{WT/lacZ} mice are associated with blood vessels as previously described in PFBC patients and mouse models [19, 26, 32]. To visualize calcifications, we used immunofluorescent labeling of osteopontin, a bone matrix protein previously reported to be deposited in calcifications in the brain [43, 49]. Immunofluorescent co-staining of brain sections from male and female *Xpr1*^{WT/lacZ} mice with osteopontin and CD31, an endothelial cell marker, revealed that calcifications were associated with vasculature and increased in size with age (Figure 1C). Notably, calcifications were smaller in *Xpr1*^{WT/lacZ} females compared with the age-matched *Xpr1*^{WT/lacZ} males. As described in other PFBC mouse models [43, 49, 50], in addition to osteopontin, these calcifications also contained other bone matrix proteins such as osteocalcin, cathepsin K, and amyloid precursor protein (APP) (Figure S2a,b). APP immunostaining is used to detect

sites of axonal injury [51]. However, the APP immunoreactivity was restricted to vascular calcifications in *Xpr1*^{WT/lacZ} mice. High magnification images of CD31 staining revealed an occasional loss of CD31 immunoreactivity in vessel segments covered with osteopontin-positive nodules (Figure S3a, white arrows), suggesting that in these regions the endothelial lining could be discontinuous. However, vascular segments with loss of CD31 were perfused as assessed by the presence of intravenously injected 70-kDa dextran conjugated to Texas Red (Figure S3a) but showed tortuosity (Figure S3a,b, white arrowhead) and irregularities in lumen diameter (Figure S3b, white arrow). The 70-kDa dextran-Texas Red did not extravasate into the parenchyma, suggesting that the observed vascular changes in *Xpr1*^{WT/lacZ} mice were not accompanied by BBB breakdown (Figure S3a,b).

We next assessed which vascular segments become calcified in *Xpr1*^{WT/lacZ} mice. To visualize the vascular network, including arterioles and calcifications, we used antibodies against collagen IV, α -smooth muscle actin (ASMA), and osteopontin, respectively. Calcifications were associated only with ASMA-positive arterioles and covered with basement membrane (BM; Figure 1D, white arrowheads). Occasionally, calcified vessel segments showed loss of ASMA immunostaining (Figure S3c). To confirm that calcifications develop on arterioles, we used an antibody against elastin, an extracellular matrix protein deposited only around vessels with vascular smooth muscle cell (VSMC) coverage (i.e., arteries, arterioles) and antibody against laminin subunit α 1 (LAMA1), a protein expressed by vessel-associated fibroblasts and used to identify arterioles in mouse brain [52]. Osteopontin-positive calcifications were associated with elastin-positive vessels (Figure S3d) and LAMA1-positive vessels (Figure S3e) confirming that calcified vessels are arterioles. Of note, podocalyxin immunoreactivity, in addition to CD31, was lost in vessel segments covered with calcifications (Figure S3f, yellow arrowheads), suggesting a phenotypic change or loss of endothelial cells.

FIGURE 1 Characterization of ectopic brain vascular calcifications in *Xpr1*^{WT/lacZ} mice. (A) Histological staining of brain sections of 16-month-old *Xpr1*^{WT/lacZ} mice showing nodules positive for staining with hematoxylin and eosin (HE), periodic acid-Schiff (PAS), alcian blue (AB), von Kossa (VK), and alizarin red (AR) which are absent in controls. Black arrows indicate the nodules shown in the inset at higher magnification. Scale bars: 200 μ m, 25 μ m inset. $n = 3$ mice. (B) Quantification of Pi levels in the CSF of *Xpr1*^{WT/WT} and *Xpr1*^{WT/lacZ} mice ($P = 0.0010$). $n = 4-5$ mice. Data are presented as mean \pm SD (C) Immunofluorescence analysis of calcifications in 7- to 16-month-old female and male *Xpr1*^{WT/lacZ} mice. Osteopontin-positive calcifications (red) are associated with vessels (white). Images are acquired at midbrain region. Scale bar: 100 μ m. $n = 4-5$ mice per stage. (D) Osteopontin-positive calcifications (red) are associated with arterioles (ASMA positive, cyan) in the thalamus of 16-month-old *Xpr1*^{WT/lacZ} mice. A white dotted line drawn with reference to ASMA staining shows localization of calcification around ASMA positive vessel. White arrowheads point to the coverage of BM (Collagen IV, yellow) around calcifications. Scale bar: 100 μ m. $n = 3-5$ mice. (E) TEM image in 16-month-old *Xpr1*^{WT/lacZ} male mice showing arteriole-associated calcification in the thalamus, which appears as layered nodule with electron-dense and rugged edges. Near calcification signs of tissue rarefaction (blue arrows) and a myelin balloon (black asterisk) were seen. The calcified arteriole presents with thickened BM (pink arrowhead). Dark microglia (MG) (white arrow) was observed adjacent to the calcification. The orange and yellow dotted box surrounds magnified regions, showing BM coverage (red arrows) around the calcification. Endothelial cell (black arrow) with intact cell-cell junction (black arrowhead) is separated from calcification by the BM (red arrow). Adjacent to the calcification, VSMC (red asterisk) is also seen. Note the absence of BM between VSMC and calcification. The pink dotted box surrounds the magnified region showing another nodule, with electron-dense and rugged edges, adjacent to a cell (pink asterisk). Note the absence of BM between the cell and the nodule. VL, vessel lumen. Scale bars: 10 μ m, 5 μ m inset. (F) Selected SEM images from the array show layered calcification and continuous BM (red arrows) around the calcification. VSMC (red asterisk) is observed adjacent to the calcification and contains electron-dense accumulations (red arrowhead). Scale bar: 5 μ m. $*P < 0.05$.

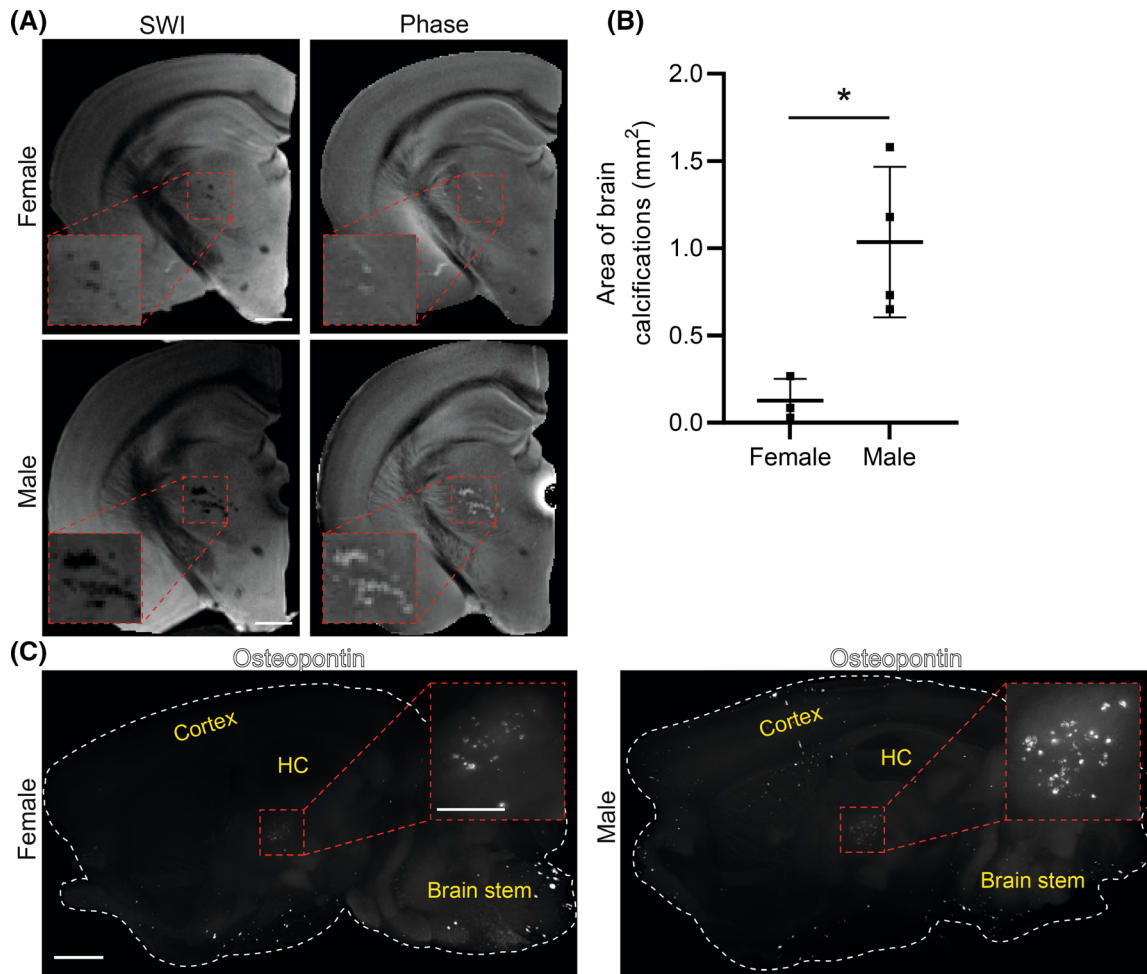


FIGURE 2 Sexually dimorphic development of brain calcification in *Xpr1*^{WTlacZ} mice. (A) A brain section from SWI and corresponding phase image showing calcification as hypointensities (red dotted box) in the thalamus of 16-month-old male and female *Xpr1*^{WTlacZ} mice and diamagnetic nature, calcification, of the hypointensities observed in SWI, respectively. Insets show magnified view of the boxed region in the corresponding image. Scale bar: 1000 μ m. (B) Quantification of calcification load in *Xpr1*^{WTlacZ} female and male mice from SWI images. $P = 0.0179$, $*P < 0.05$. Each data point represents the sum of area of calcification from one hemisphere. $n = 3$ *Xpr1*^{WTlacZ} female and four *Xpr1*^{WTlacZ} male. Data are presented as mean \pm SD. (C) Osteopontin labeled calcifications (white) in cleared hemispherized brain of a 16-month-old *Xpr1*^{WTlacZ} female and male mouse. Inset shows higher magnification of the calcified region in the thalamus. A white dotted line marks the outline of the brain. The overview images are compiled of selected sequential optical slices. Higher magnification (inset) is a maximum-intensity view of the calcified region. Punctiform signal visible in the cortex of male mice is due to non-specific secondary antibody aggregates. HC, hippocampus. Scale bars: 1000 μ m overview and 500 μ m inset. $n = 3-4$ mice.

Immunofluorescently labeled collagen IV conspicuously outlined calcifications (Figure 1D, white arrowheads), suggesting that these calcifications develop within the vessel wall. Transmission electron microscopy (TEM) imaging of the thalamus of 16-month-old *Xpr1*^{WTlacZ} mice confirmed arteriolar calcification, where the calcifications appeared as layered nodules surrounded by the BM (Figure 1E, orange and yellow inset, red arrows; Figure S4, red inset, red arrows). This was corroborated by array tomography scanning electron microscopy (AT-SEM), where 3D reconstruction of the images showed continuous BM surrounding calcification (Figure 1F, Video S1). Continuous BM was detected between the calcification and endothelial cell (Figure 1E, orange inset, black arrow), suggesting that calcifications develop within the VSMC layer

(Figure 1E, orange inset). The presence of endothelial layer under calcification (Figure 1E, orange inset, black arrow) suggests that poor CD31 and podocalyxin labeling of endothelium covered with osteopontin positive nodules (Figure S3a,f) could reflect phenotypic changes in the endothelium. The edges of the calcification were rugged and electron dense (Figures 1E and S4). VSMC containing electron-dense accumulations were located adjacent to the lamellar nodule (Figure 1E, orange inset, red asterisk). Between the nodule and VSMC we could not identify the BM. In addition, the BM surrounding the calcified vessel was thickened (Figure 1E, pink arrowhead). The parenchyma adjacent to the calcified vessel showed foci of rarefaction (Figure 1E, blue arrows). Another smaller nodule surrounded by a cell was present (Figure 1E, pink inset)

in the image, which could be part of the lamellar nodule described above. There was no identifiable BM separating the cell (Figure 1E, pink inset, pink asterisk) from the nodule. Thus, *Xpr1^{WT/lacZ}* mice present with vascular calcifications, which develop in the smooth muscle cell layer of arterioles in the thalamus.

3.3 | Sexual dimorphism in development of calcifications in *Xpr1^{WT/lacZ}* mice

The confocal laser scanning microscopy analysis of calcifications pointed toward the sexual dimorphism in development of vascular calcification in *Xpr1^{WT/lacZ}* mice (Figure 1C). To visualize calcifications in the whole brain, we performed ex vivo susceptibility weight (SW) imaging and phase analysis, which confirmed the diamagnetic nature of lesions (i.e., presence of calcium; Figure 2A). Thalamus-restricted hypointensities in SW images and hyperintensities (positive phase shifts) in phase images (Figure 2A), confirmed our previous observations of thalamus-restricted calcifications in *Xpr1^{WT/lacZ}* mice. Quantification of calcification load in *Xpr1^{WT/lacZ}* mice showed a significantly higher calcification load in males compared with females (Figure 2B).

In addition to the SW imaging, we performed whole-brain immunostaining using an antibody against osteopontin followed by tissue clearing using the iDISCO protocol [37]. Whole brain imaging using a light-sheet microscope [38] confirmed that calcifications are confined to the thalamus, and female *Xpr1^{WT/lacZ}* mice present with less calcifications as compared with *Xpr1^{WT/lacZ}* male mice (Figure 2C, Videos S2 and S3). Osteopontin is also expressed by neurons of precerebellar nuclei [53], which was visible in brain stem neurons in whole brain staining in both *Xpr1^{WT/lacZ}* (Figure 2C, Videos S2 and S3) and wild-type mice (Video S4). However, strong osteopontin signal originating from vascular calcifications in the thalamus was only seen in heterozygous *Xpr1* animals.

Thus, our data show that both male and female *Xpr1* heterozygous mice develop vascular calcifications, however, with age, calcifications grow significantly larger in males.

3.4 | Microangiopathy and vessel tortuosity in *Xpr1^{WT/lacZ}* mice

In addition to the presence of vascular calcifications, the analysis of TEM images pointed to changes in endothelial cells, VSMCs, and BM in *Xpr1^{WT/lacZ}* mice (Figure 3A–C) indicating microangiopathy. We observed vessels with convoluted (Figure 3A) or narrowed lumen with swollen endothelium (Figure 3B). Arterioles were often associated with thickened VSMC (Figure 3A, red arrows, inset; Figure S5a), degenerating VSMC

(Figure 3C, red arrow), or with VSMC containing swollen mitochondria (Figure 3C, red inset) and had a thickened BM (Figure 3C, red arrowhead). These abnormalities were absent in age-matched wild-type mice (Figure S5a). In addition, several capillaries of *Xpr1^{WT/lacZ}* mice had thickened BM (Figure S5b, red arrow) and swollen endothelium (Figure S5b, red asterisk). However, we did not observe calcification of capillaries in *Xpr1^{WT/lacZ}* mice. The endothelial cell–cell junctions appeared intact in *Xpr1^{WT/lacZ}* mice, even in calcified regions (Figure 1E, orange inset, black arrowhead). In addition, the age-related degenerating features observed in *Xpr1^{WT/lacZ}* mice such as myelin balloons (Figure 1E, black asterisk) and lysosome accumulations (Figure S5a, red arrows) were also present in *Xpr1^{WT/WT}* mice (not shown).

Morphological changes in the vasculature observed in TEM images could be associated with vascular inflammation as the endothelium in *Xpr1^{WT/lacZ}* mice showed an increased expression of intracellular adhesion molecule 1 (ICAM-1; Figure 3D), a leukocyte adhesion molecule upregulated in endothelium in response to inflammatory stimuli [54]. Quantification of ICAM-1 coverage of blood vessels in deep brain region showed a higher ICAM-1 coverage in *Xpr1^{WT/lacZ}* mice as compared with age-matched controls, although the difference was not statistically significant (Figure S5c).

Visualization of vasculature using antibodies against ASMA and collagen IV revealed tortuous penetrating arterioles in the cortex (Figure 3E), demonstrating that *Xpr1^{WT/lacZ}* mice present vascular changes also in other brain regions. Although analysis of the retina did not reveal calcification of arterioles in *Xpr1^{WT/lacZ}* mice (Figure S5d), they frequently showed alterations in the vascular network in the superficial layer (Figure S5e).

Thus, *Xpr1* heterozygosity leads to microangiopathy and vascular inflammation in the brain.

3.5 | Glial reactivity in *Xpr1^{WT/lacZ}* mice

Vascular calcifications surrounded by astro- and microgliosis have been reported in PFBC patients and mouse models [19, 26, 43, 49, 50]. This prompted us to investigate whether similar reactivity of astrocytes and microglia can be detected also in *Xpr1^{WT/lacZ}* mice. Consistent with previous studies in PFBC mouse models and human patients, strongly GFAP positive astrocytes surrounded vascular calcifications in *Xpr1^{WT/lacZ}* mice (Figure 4A). Furthermore, astrocytes in the near vicinity to calcified vessels showed loss of connexin 43 (Figure 4B), a gap junction protein, mislocalization of aquaporin 4 (Figure 4C, yellow arrowheads), an astrocyte endfeet protein, and were positive for complement 3 (C3) (Figure 4D, white arrowheads), a marker for neurotoxic astrocytes, suggesting altered astrocyte homeostasis.

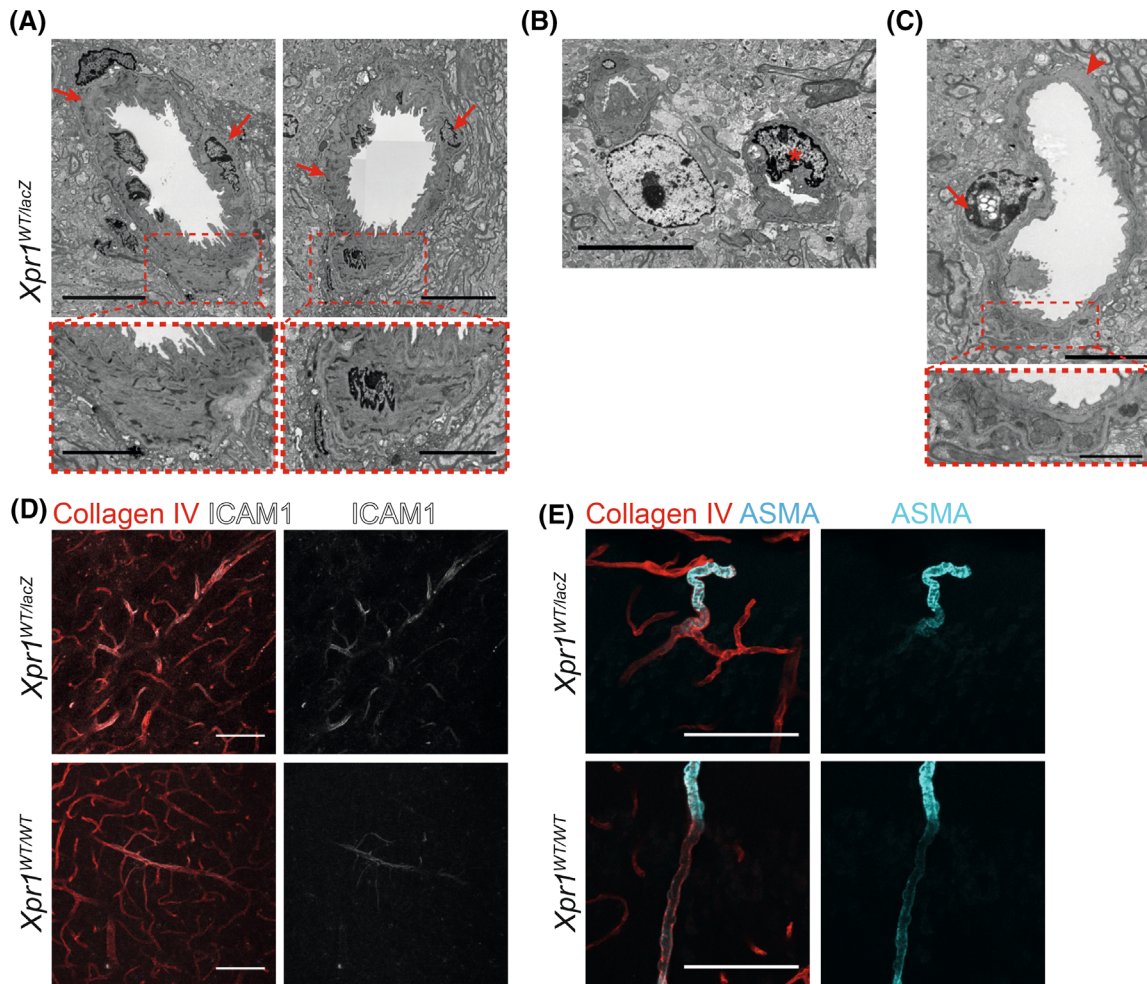


FIGURE 3 Microangiopathy in *Xpr1*^{WT/lacZ} mice. (A–C) TEM images of the thalamus of 16-month-old *Xpr1*^{WT/lacZ} male mice showing vascular alterations. (A) Vessels with convoluted lumen associated with altered VSMC (red arrows). Red dotted box surrounds the thickened VSMC in magnified view. Scale bars: 10 μ m, 5 μ m magnified view. (B) Vessels with narrowed lumen. Red asterisk labels swollen endothelial cell. Scale bar: 10 μ m. (C) Image of a vessel associated with degenerating VSMC (red arrow) and thickened BM (red arrowhead). Scale bar: 5 μ m. (D) Immunohistochemical staining of deep brain region showing increased vascular ICAM-1 staining (white) in *Xpr1*^{WT/lacZ} mice. Scale bar: 100 μ m. (E) Tortuous arterioles (ASMA, cyan) in the cortex of 16-month-old *Xpr1*^{WT/lacZ} mice. Scale bar: 100 μ m. For IHC $n = 3$ mice.

Calcifications were also surrounded by strongly IBA1 positive microglia expressing CLEC7A (Figure 5A, pink arrowheads), a marker for calcification-associated microglia [44]. Consistent with increased microglial reactivity, we detected enhanced proliferation of microglia in the deep brain of *Xpr1*^{WT/lacZ} mice (Figure S6a). However, microglial activation was not confined to calcifications and was also observed in other brain regions (e.g., cortex, white matter, midbrain) of *Xpr1*^{WT/lacZ} mice (Figure S6b). In addition, we detected microglia exhibiting electron-dense cytoplasm and swollen mitochondria (Figures 1D and 5B), a phenotype characteristic for so-called “dark” microglia associated with neurodegenerative diseases [55]. Furthermore, several microglia in *Xpr1*^{WT/lacZ} mice contained conspicuous fibrillar inclusions (Figure 5C, surrounded by red dotted line). Fibrillar bodies with a similar appearance were found in the thalamic neurons, of both wild type and *Xpr1*^{WT/lacZ}

mice (Figure S6c, red arrow). However, the presence of fibrillar inclusion bodies in microglia was detected only in *Xpr1*^{WT/lacZ} mice. Interestingly, in one instance, we observed gap junctions in between two microglia (Figure S6d, inset) in *Xpr1*^{WT/lacZ} mice, an indication of inflammatory state of microglia [56].

Taken together, in addition to glial reactivity around calcifications, *Xpr1*^{WT/lacZ} mice present with widespread microglial activation.

3.6 | *Xpr1*^{WT/lacZ} mice present with altered acoustic startle response

We next performed a battery of tests to assess behavior in *Xpr1*^{WT/lacZ} mice. No difference in behavior between *Xpr1*^{WT/lacZ} and *Xpr1*^{WT/WT} mice was seen in tests that assessed innate anxiety, locomotor response to a novel

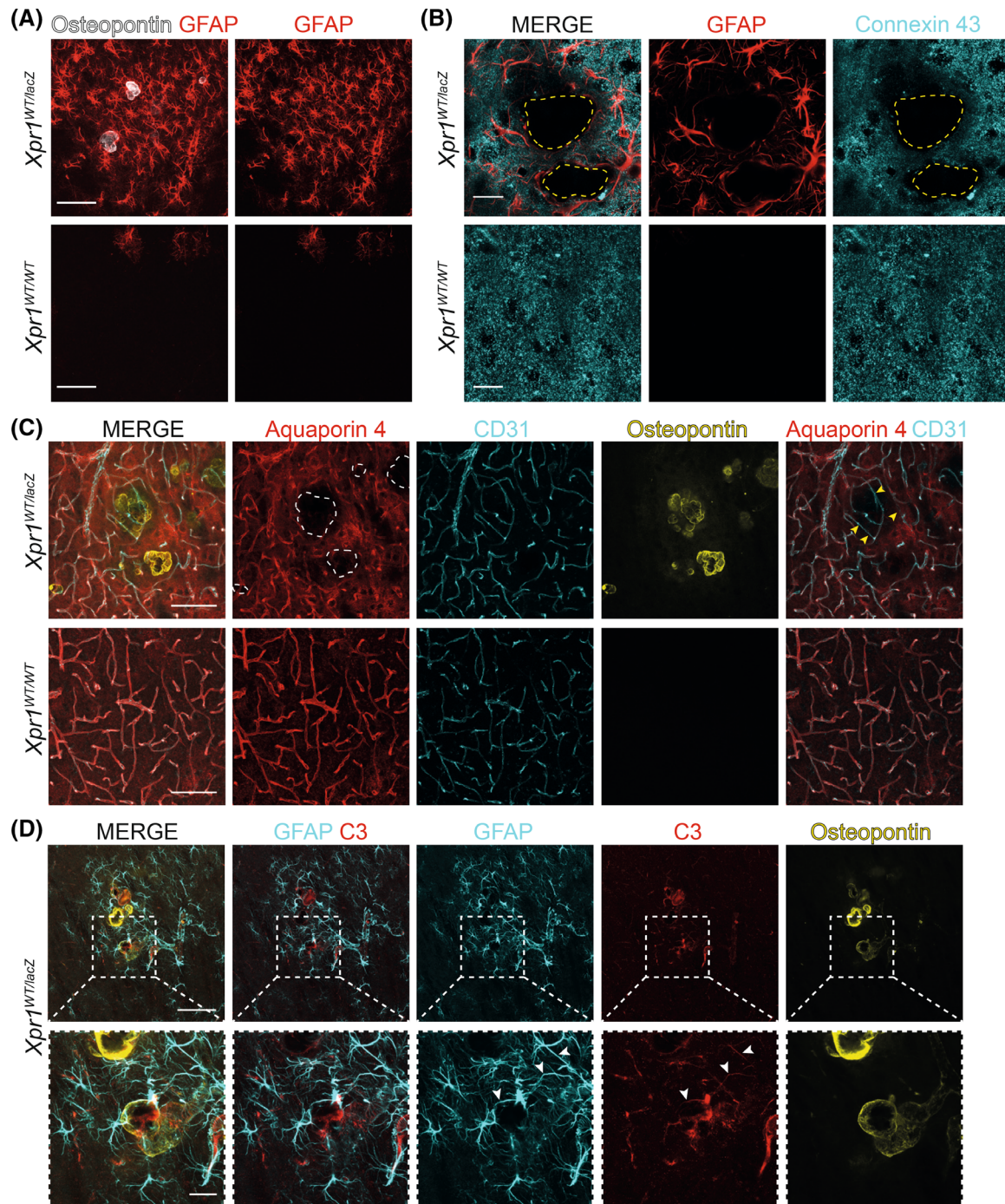


FIGURE 4 Reactive astrocytes in *Xpr1^{WTlacZ}* mice surround vascular calcifications. (A) Strongly GFAP-positive astrocytes (red) in the deep brain region of 16-month-old *Xpr1^{WTlacZ}* mice. GFAP-positive astrocytes were surrounding calcifications (white) and were also widespread in the deep brain region. Scale bar: 100 μ m. (B) Reduced connexin 43 expression (cyan) observed in regions surrounding calcifications (yellow dotted line) in *Xpr1^{WTlacZ}* mice. Scale bar: 25 μ m. (C) Mislocalized aquaporin 4 (red) from astrocyte endfeet in near vicinity to calcified vessels (yellow, marked with white dotted line). Blood vessels are visualized with antibody detecting CD31 (cyan). Some vessel segments lacked aquaporin 4 coverage (yellow arrowheads). Scale bar: 100 μ m. (D) GFAP-positive astrocytes (cyan) express C3 (red) around osteopontin-positive calcifications (yellow). Higher magnification image shows colocalization of GFAP and C3 expression (white arrowheads). Scale bars: 100 μ m, 25 μ m higher magnification. For IHC $n = 3$ mice.

environment, spatial learning and memory, and social interaction (Figure S7a–d).

In addition, we assessed sensorimotor gating in *Xpr1^{WTlacZ}* mice by measuring the prepulse inhibition (PPI) of the acoustic startle reflex. This test measures the

reduction in startle response to an acoustic stimulus (pulse), when the subject is exposed to a weak acoustic stimulus (prepulse) shortly before the main stimulus [57]. We found that *Xpr1^{WTlacZ}* mice presented an increased mean PPI compared with controls (Figure 6A). Further

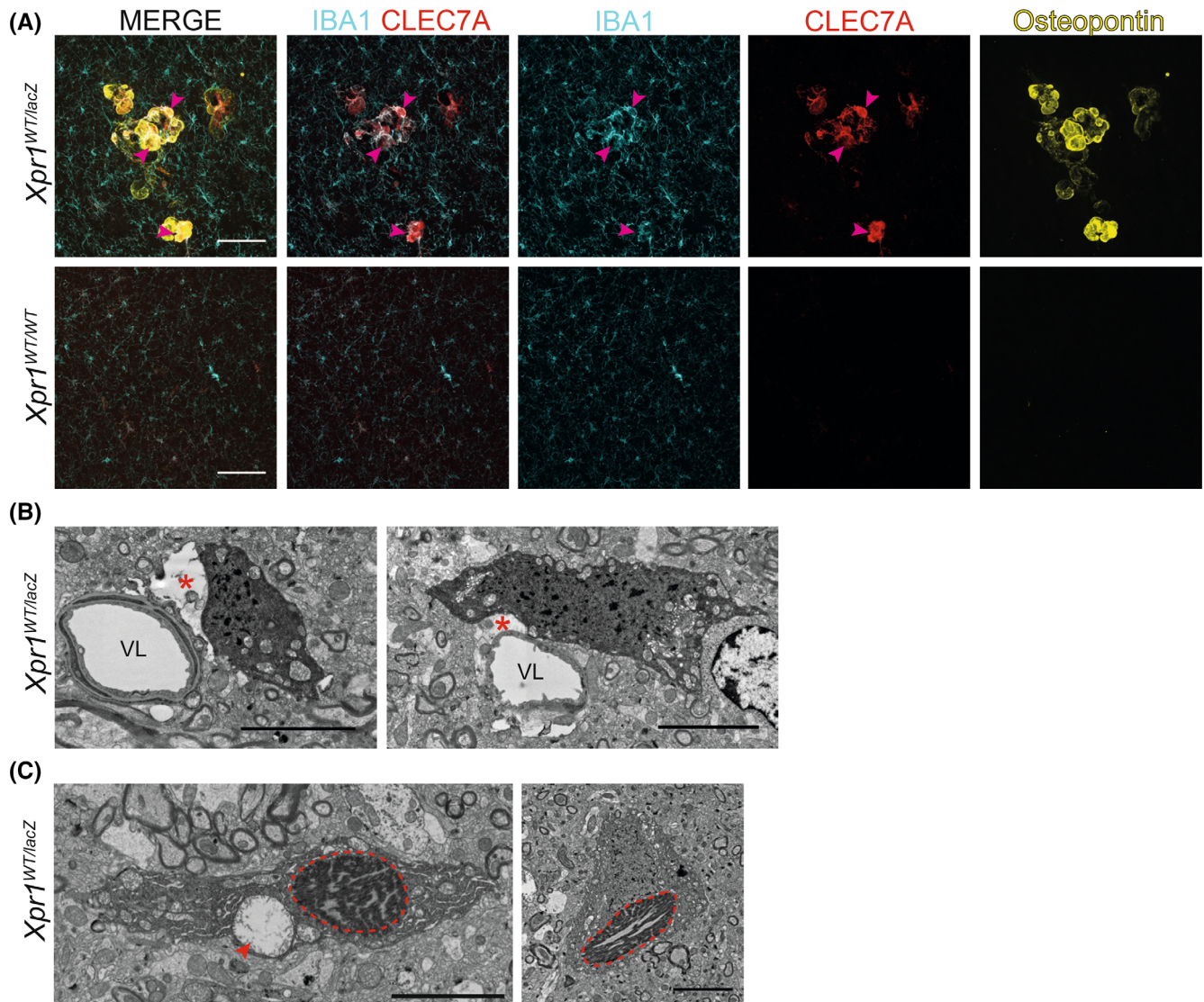


FIGURE 5 Activated microglia in the brain of *Xpr1*^{WT/lacZ} mice. (A) Immunofluorescent staining showing expression of CLEC7A (red) in IBA1-positive microglia (cyan) surrounding osteopontin-positive calcifications (yellow). A few microglia surrounding calcifications were strongly positive for CLEC7A and IBA1 (pink arrows). Scale bar: 100 μ m. For IHC $n = 3$ mice. (B,C) TEM images showing (B) dark microglia and (C) microglia containing fibrillar inclusion (surrounded by red dotted line) in *Xpr1*^{WT/lacZ} mice. Note the presence of swollen astrocyte end-feet (red asterisk) adjacent to dark microglia (B) and swollen mitochondria (red arrowhead) in microglia with fibrillar inclusion (C). VL, vessel lumen. Scale bar: 5 μ m.

analysis of the data showed that *Xpr1*^{WT/lacZ} mice had significantly elevated PPI response to lower-intensity pulses of 100 and 110 dB (Figure 6B). However, comparison of the response to prepulse alone and to acoustic startle to pulse showed that *Xpr1*^{WT/lacZ} mice had a significantly elevated acoustic startle response to pulses of intensities 100 and 110 dB (Figure 6C) and to high-intensity prepulse of 83 dB (Figure 6D) compared with controls. Thus, the increased mean PPI in *Xpr1*^{WT/lacZ} mice could be confounded by differences in their basal startle response. These alterations in acoustic startle response and reaction to prepulse did not differ between control and *Xpr1*^{WT/lacZ} mice at the age of 7 months (Figure S7e,f). The startle response of control animals at both ages was similar (Figure S7g,h), with young control

mice showing higher reaction to prepulse of 83 dB (Figure S7h). Therefore, observed changes in aged *Xpr1*^{WT/lacZ} mice cannot be attributed to age but are a read-out of genotype-related behavioral alteration.

4 | DISCUSSION

In this study, we show that mice heterozygous for the *Xpr1* gene present with sex-dependent growth of vascular calcifications in the VSMC layer around thalamic arterioles, thus recapitulating the pathological hallmark of PFBC patients, that is, calcification of blood vessels. Furthermore, *Xpr1* heterozygous mice show additional vascular alterations such as narrowed lumen and thickening

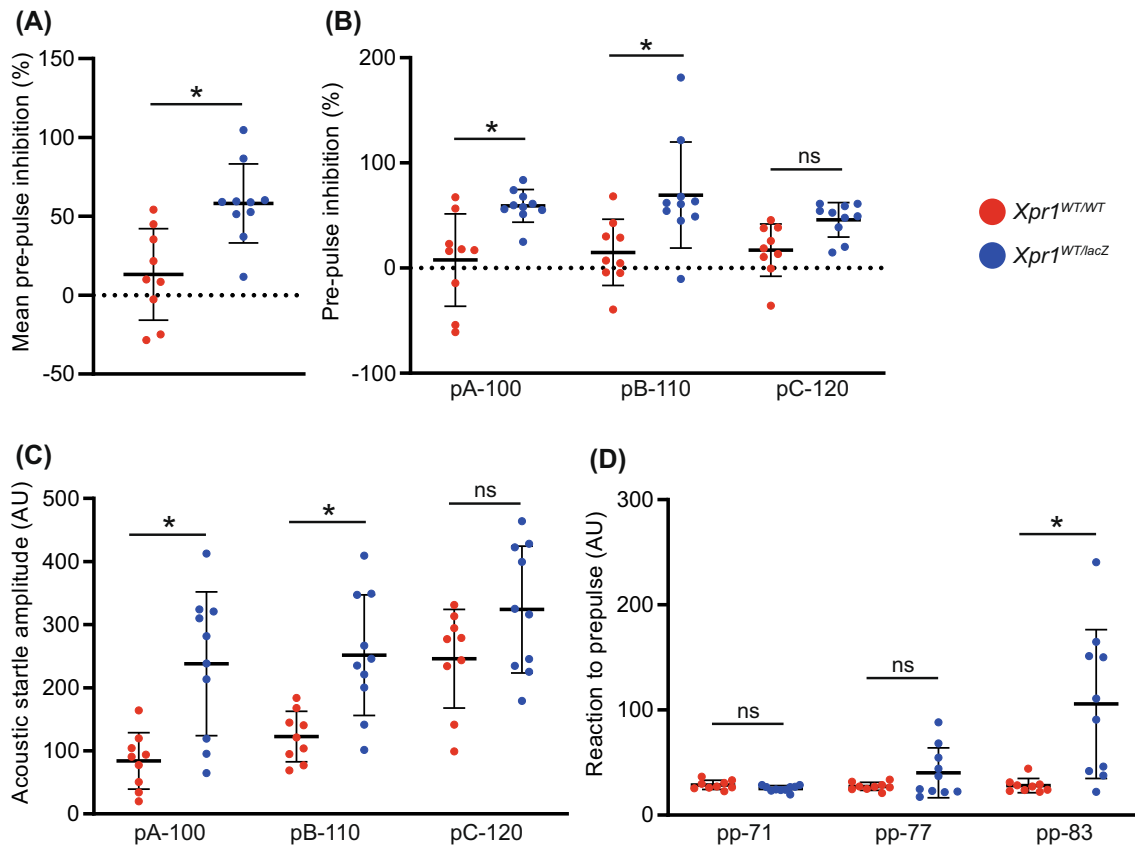


FIGURE 6 Behavioral analysis of *Xpr1*^{WT/lacZ} mice. (A) Analysis from pre-pulse inhibition test, where the mean PPI is expressed as percentage and calculated from the reflex outcomes of a combination of three different prepulses and three different pulses ($P = 0.0021$). (B) Percentage pre-pulse inhibition exhibited by mice when subjected to different pulses (100, 110, and 120 dB), each pulse is presented as a mean of combination with three different prepulses (pp71, pp77, and pp83) (pA $P = 0.0040$; pB $P = 0.0022$; pC $P = 0.1804$). (C) The acoustic startle reflex of mice measured in arbitrary units (AU) plotted against three different pulses—100, 110, and 120 dB (pA $P = 0.0007$; pB $P = 0.0051$; pC $P = 0.1445$). (D) Startle reflex of mice to three different prepulses (pp71, pp77, and pp83) measured in arbitrary units (AU) plotted against each prepulse (pp71 $P = 0.9938$; pp77 $P = 0.7599$; pp83 $P = <0.0001$). $n = 9$ *Xpr1*^{WT/WT} and $n = 10$ *Xpr1*^{WT/lacZ} mice. Data are presented as mean \pm SD. * $P < 0.05$. ns, not significant.

of the BM and microgliosis, independent from vascular calcification. The presence of cerebrovascular pathology in *Xpr1* heterozygous mice warrants further studies to determine whether the observed changes and microgliosis are also present in PFBC patients. Also, further insights are needed on whether these changes could lead to ischemic events, inflammation, and neurodegeneration.

Our analyses confirm and extend previous histopathological observations of age-dependent vascular calcifications described in other mouse models of PFBC and autopsies of PFBC cases [19, 20, 26, 32, 33]. In *Xpr1*^{WT/lacZ} mice, mulberry-shaped vascular calcifications are confined to arterioles (Figures 1D and S3d,e) and encapsulated in BM (Figures 1D,E and S4), demonstrating that these calcifications grow at the vessel wall of the arterioles in the VSMC layer. Analysis of AT-SEM datasets of a calcified vessel segment confirmed these observations (Figure 1F, Video S1). Calcifications were separated from the endothelium by the BM and were residing in the VSMC layer (Figure 1E), suggesting that vascular calcification due to *Xpr1* heterozygosity is initiated by either VSMC death or

phenotypic change, both being suggested to initiate vascular calcification [58, 59].

Xpr1 heterozygosity leads to reduced Pi levels in the CSF (Figure 1B). On the contrary, loss of *Slc20a2* and *SLC20A2* mutations lead to increased Pi levels in the CSF [33, 60] and it has been suggested that this causes local deposition of calcium phosphate in the glymphatic space and subsequent calcification of vessels [33]. Thus, if the elevated Pi in the CSF drives vascular calcification, then the pathomechanism likely differs between LOF of *SLC20A2* and *XPR1*. Nevertheless, studies have shown that *SLC20A2* and *XPR1* co-operate and regulate intracellular Pi levels [7]. Whether histopathological alterations in *Xpr1* heterozygous mice are caused by intracellular alterations in Pi metabolism and/or changes in Pi concentration in the CSF should be addressed in future studies.

Several arterioles and capillaries in *Xpr1*^{WT/lacZ} mice had a thickened BM, narrowed lumen, and swollen endothelial cells (Figures 3 and S5). In addition, cortical arterioles showed tortuosity (Figure 3E). We also detected reduced ASMA expression and ultrastructural changes in

VSMC, indicative of phenotypic change and degeneration (Figures S3c, S5a, and 3A–C). These changes were not accompanied by alterations in endothelial cell–cell junctions nor increased transcytosis consistent with the intact BBB (Figures 1E and S3a). However, reduced CD31 and podocalyxin staining of calcified vessel segments (Figure S3a,f) is an indication of a phenotypic change of vascular cells, which eventually could lead to microvascular rarefaction, observed also in a PFBC autopsy case [26]. Microangiopathy in the skin has been reported in PFBC patients, including one *XPR1* mutation carrier [61, 62]. Also, degeneration of VSMC without calcification has been observed in PFBC brain [63]. However, no data is available on brain pathology in *XPR1* mutation carriers. Acute ischemic stroke and decreased cerebral blood flow have been reported in several patients with PFBC mutations [27, 29, 64–67]. Thus, accumulating evidence points to widespread vascular changes in PFBC patients and advocates for studies focused on the cerebrovascular reactivity and perfusion of PFBC patients. The retinal vasculature showed an altered pattern in the superficial layer in *Xpr1^{WT/lacZ}* mice (Figure S5e). Interestingly, microphthalmia and cataracts were reported in *Slc20a2^{-/-}* mice [33], however, whether these mice present with abnormalities in retinal vasculature has not been reported. No ophthalmic findings were found in *SLC20A2* and *PDGFB* mutation carriers [68].

Along with brain vascular calcification, glial cell reactivity has been a consistent observation in different PFBC mouse models and human autopsy cases [21, 26, 43, 49, 50]. Our data corroborates and extends these findings (Figure 4 and Figure 5). In *Xpr1^{WT/lacZ}* mice, the astrocyte reactivity pattern, based on the GFAP expression around calcifications, was similar to that of *Slc20a2^{-/-}* mice and *SLC20A2* mutation carriers (Figure 4A) [26, 50]. In addition, we report reduced expression of connexin 43 (Figure 4B) and mislocalization of aquaporin 4 from astrocyte endfeet (Figure 4C) indicative of altered astrocyte homeostasis [69, 70]. Microglia surrounding calcifications were strongly IBA1 positive and expressed CLEC7A (Figure 5A), a marker previously identified in calcification-associated microglia [49]. In addition, the TEM imaging revealed the presence of so-called “dark microglia”, identified by their electron-dense cytoplasm and large mitochondria (Figures 1E and 5B) [55]. CLEC7A-positive microglia were detected only at the site of calcifications but microglia presenting strong IBA1 reactivity and altered morphology were detected in several brain regions which all lacked vascular calcifications. Also, widespread appearance of “dark microglia” in the TEM images is suggestive of a global microglial reactivity in *Xpr1^{WT/lacZ}* mice. Dark microglia were initially identified based on the appearance in TEM images (e.g., electron-dense cytoplasm and hence the name) in mouse brain and associated with pathological conditions and aging and have also been shown in human brain

[55, 71]. Thus, the appearance of microglia in *Xpr1^{WT/lacZ}* mice with ultrastructural similarities to those described in other pathologies is suggestive of parenchymal changes. In addition, we observed peculiar fibrillar inclusions in microglia only in *Xpr1^{WT/lacZ}* mice (Figure 5C), suggestive of microglial phagocytosis of neurons containing these fibrillar bodies. Morphologically similar inclusions have been described in thalamic neurons in aged mice, an epileptic mouse strain, and osteopontin (*Spp1*)-deficient mice after excitotoxic insult but the nature of these inclusions is not known [72–74]. Curiously, in zebrafish—*xpr1b*, an orthologue of XPR1, is instrumental for the differentiation of tissue-resident macrophages and microglia [75]. Cell type specific knockout of *Xpr1* should clarify whether microgliosis is due to cell autonomous changes in microglia or changes in neural tissue due to the loss of the *Xpr1* allele or, both.

Clinical manifestation of PFBC patients is heterogeneous and could include motor, cognitive deficits, and/or psychiatric symptoms [16]. Behavioral analysis of mouse models of PFBC also suggested the presence of variety of behavioral phenotypes in different models [21, 43, 76]. Here, we report that *Xpr1^{WT/lacZ}* mice present with higher acoustic startle response and response to prepulse in PPI test (Figure 6). Increased acoustic startle response in rats after delivery of yohimbine, a drug that elicits anxiety in healthy individuals, and startle reactivity correlating to anxiety in humans are suggestive of a link between anxiety and changes in the startle response [19, 77]. Vascular calcifications in the thalamus of *Xpr1^{WT/lacZ}* mice could alter the connectivity of thalamic neurons, thereby causing changes in the sensory processing via thalamic nuclei. Alternatively, the increased anxiety could be a result of intrinsic changes in neurons in *Xpr1^{WT/lacZ}* mice. Our analysis did not reveal remarkable ultrastructural changes in thalamic neurons in *Xpr1^{WT/lacZ}* mice. Earlier studies have reported that downregulation of XPR1 due to virus infection in SY5Y human neuroblastoma cells leads to cell apoptosis which can be avoided by expression of mouse XPR1 [78]. Further studies are needed to understand potential changes in connectivity of thalamic neurons resulting in behavioral alteration in *Xpr1^{WT/lacZ}* mice and whether these changes are intrinsic to neurons.

Brain vascular calcification in *Xpr1^{WT/lacZ}* mice was detected in both sexes (Figure 2), a phenotype consistent with previously reported demographics for PFBC [16]. However, using different imaging approaches (i.e., ex vivo MRI, whole brain and slice immunofluorescence imaging) we observed increased calcification load in males as compared with females. So far, no mouse model of PFBC has been reported to present sexual dimorphism in calcification progression and load. However, studies in PFBC patients have suggested that male gender could contribute to the higher calcification score [79]. Sex differences and sex hormones influence cardiovascular calcification and future studies should

address whether reduced vascular calcification in female *Xpr1^{WTlacZ}* mice is due to the protective effect of female sex-hormones [80].

In summary, our study provides insights into the pathogenesis of cerebrovascular calcifications and associated vascular and microglial changes in PFBC. Further research is needed to understand whether vascular and microglial changes in *Xpr1* heterozygous mice present a reaction to neural damage or are caused by a cell-autonomous role of XPR1 in microglial and vascular cells. In addition, our findings warrant studies that assess brain inflammation, cerebrovascular reactivity, and blood flow in PFBC patients.

AUTHOR CONTRIBUTIONS

Upasana Maheshwari and Annika Keller conceptualized and designed the study. Upasana Maheshwari, José M. Mateos, Virgil Tamatey, Sucheta Sridhar, Alejandro Restrepo, Sheng-Fu Huang, Johanna Schaffenrath and Sebastian A. Stifter performed the experiments. The results were interpreted by Annika Keller, Upasana Maheshwari, Ulrike Weber-Stadlbauer, Ruiqing Ni, Flora Szeri, Pim A. de Jong, Melanie Greter, and Huiberdina L. Koek. Upasana Maheshwari and Annika Keller analyzed and compiled the data. Upasana Maheshwari and Annika Keller wrote the manuscript. All authors read and commented on the manuscript.

ACKNOWLEDGMENTS

The authors would like to thank the Center for Microscopy and Image Analysis, University of Zurich for granting access to the microscopes and for sample preparation and acquisition of electron microscopy images. Specifically, Ursula Lüthi, Bogdana Todorovic, Carmen Kaiser, Nicolas Schilling and Johannes Riemann. We thank Irina Abakumova, Institute of Neuropathology, University Hospital Zurich for assisting in histology. We thank Vasil Kecheliev for his help with SWI-MRI image acquisition. Blood plasma analyses were done by Zurich Integrative Rodent Physiology, University of Zurich. We thank Prof. Robert Mecham, Washington University School of Medicine in St. Louis for sharing anti-elastin antibody and Prof. Lydia Sorokin, Institute of Physiological Chemistry and Pathobiochemistry, University of Muenster, Germany for sharing anti-LAMA1 antibody.

FUNDING INFORMATION

This study was financed with grants to A.K. from the Swiss National Science Foundation (310030_188952), the Swiss Multiple Sclerosis Society, Dementia Research Switzerland – Synapsis Foundation and Choupette Foundation (2019-PI02), and Novartis Free-Novation. Grants to F.S. from National Research, Development and Innovation Office (FK131946), New National Excellence Program of the Ministry for Innovation and Technology from the source of the NKFIH (ÚNKP-22-5-SE-2), and The Hungarian Academy of

Sciences (Bolyai János Fellowship BO/00730/19/8). F.S. and V.T. are members of the international Network on Ectopic Calcification (INTEC).

CONFLICT OF INTEREST STATEMENT

The authors declare that they have no competing interests.

DATA AVAILABILITY STATEMENT

The raw data that support the findings of this study are available from the corresponding author upon reasonable request.

ETHICS STATEMENT

Animal experiments were carried out in accordance with the protocols approved by the cantonal veterinary office Zurich under permit numbers ZH151/2017 and ZH194/2020.

ORCID

Upasana Maheshwari  <https://orcid.org/0000-0001-7516-3099>

Ruiqing Ni  <https://orcid.org/0000-0002-0793-2113>

Virgil Tamatey  <https://orcid.org/0000-0002-0066-4945>

Annika Keller  <https://orcid.org/0000-0003-1466-3633>

REFERENCES

1. Tailor CS, Nouri A, Lee CG, Kozak C, Kabat D. Cloning and characterization of a cell surface receptor for xenotropic and polytropic murine leukemia viruses. *Proc Natl Acad Sci U S A*. 1999; 96(3):927–32. <https://doi.org/10.1073/pnas.96.3.927>
2. Yang Q, Li J, Jiao B, Weng L. Primary familial brain calcification in a patient with a novel compound heterozygous mutation in MYORG presenting with an acute ischemic stroke: a case report. *Ann Transl Med*. 2022;10(7):423. <https://doi.org/10.21037/atm-21-4883>
3. Giovannini D, Touhami J, Charnet P, Sitbon M, Battini JL. Inorganic phosphate export by the retrovirus receptor XPR1 in metazoans. *Cell Rep*. 2013;3(6):1866–73. <https://doi.org/10.1016/j.celrep.2013.05.035>
4. Wild R, Gerasimaite R, Jung JY, Truffault V, Pavlovic I, Schmidt A, et al. Control of eukaryotic phosphate homeostasis by inositol polyphosphate sensor domains. *Science*. 2016;352(6288): 986–90. <https://doi.org/10.1126/science.aad9858>
5. Li X, Gu C, Hostachy S, Wittwer C, Jessen HJ, Fiedler H, et al. Control of XPR1-dependent cellular phosphate efflux by InsP(8) is an exemplar for functionally-exclusive inositol pyrophosphate signaling. *Proc Natl Acad Sci U S A*. 2020;117(7):3568–74. <https://doi.org/10.1073/pnas.1908830117>
6. Wilson MS, Jessen HJ, Saiardi A. The inositol hexakisphosphate kinases IP6K1 and -2 regulate human cellular phosphate homeostasis, including XPR1-mediated phosphate export. *J Biol Chem*. 2019;294(30):11597–608. <https://doi.org/10.1074/jbc.RA119.007848>
7. Lopez-Sanchez U, Tury S, Nicolas G, Wilson MS, Jurici S, Ayrygnac X, et al. Interplay between primary familial brain calcification-associated SLC20A2 and XPR1 phosphate transporters requires inositol polyphosphates for control of cellular phosphate homeostasis. *J Biol Chem*. 2020;295(28):9366–78. <https://doi.org/10.1074/jbc.RA119.011376>
8. Chen WC, Li QL, Pan Q, et al. Xenotropic and polytropic retrovirus receptor 1 (XPR1) promotes progression of tongue squamous cell carcinoma (TSCC) via activation of NF-kappaB signaling.

- J Exp Clin Cancer Res. 2019;38(1):167. <https://doi.org/10.1186/s13046-019-1155-6>
9. Akasu-Nagayoshi Y, Hayashi T, Kawabata A, Shimizu N, Yamada A, Yokota N, et al. PHOSPHATE exporter XPR1/SLC53A1 is required for the tumorigenicity of epithelial ovarian cancer. *Cancer Sci.* 2022;113(6):2034–43. <https://doi.org/10.1111/cas.15358>
 10. Bondeson DP, Paoletta BR, Asfaw A, Rothberg MV, Skipper TA, Langan C, et al. Phosphate dysregulation via the XPR1-KIDINS220 protein complex is a therapeutic vulnerability in ovarian cancer. *Nat Cancer.* 2022;3(6):681–95. <https://doi.org/10.1038/s43018-022-00360-7>
 11. Wang L. Bioinformatics analyses proposed xenotropic and polytropic retrovirus receptor 1 as a potential diagnostic and prognostic biomarker and immunotherapeutic target in head and neck squamous cell carcinoma. *Auris Nasus Larynx.* 2023;50(1):134–50. <https://doi.org/10.1016/j.anl.2022.05.018>
 12. Legati A, Giovannini D, Nicolas G, López-Sánchez U, Quintáns B, Oliveira JRM, et al. Mutations in XPR1 cause primary familial brain calcification associated with altered phosphate export. *Nat Genet.* 2015;47(6):579–81. <https://doi.org/10.1038/ng.3289>
 13. Lemos RR, Ramos EM, Legati A, Nicolas G, Jenkinson EM, Livingston JH, et al. Update and mutational analysis of SLC20A2: a major cause of primary familial brain calcification. *Hum Mutat.* 2015;36(5):489–95. <https://doi.org/10.1002/humu.22778>
 14. Ramos EM, Oliveira J, Sobrido MJ, Coppola G. Primary familial brain calcification. In: Adam MP, Everman DB, Mirzaa GM, Pagon RA, Wallace SE, Bean LJH, et al., editors. *GeneReviews (R)*. Seattle: University of Washington; 1993.
 15. Nicolas G, Pottier C, Charbonnier C, Guyant-Maréchal L, le Ber I, Pariente J, et al. Phenotypic spectrum of probable and genetically-confirmed idiopathic basal ganglia calcification. *Brain.* 2013;136(Pt 11):3395–407. <https://doi.org/10.1093/brain/awt255>
 16. Balck A, Schaake S, Kuhnke NS, Domingo A, Madoev H, Margolesky J, et al. Genotype-phenotype relations in primary familial brain calcification: systematic MDSGene review. *Mov Disord.* 2021;36(11):2468–80. <https://doi.org/10.1002/mds.28753>
 17. Wang C, Li Y, Shi L, et al. Mutations in SLC20A2 link familial idiopathic basal ganglia calcification with phosphate homeostasis. *Nat Genet.* 2012;44(3):254–6. <https://doi.org/10.1038/ng.1077>
 18. Nicolas G, Pottier C, Maltete D, Coutant S, Rovelet-Lecrux A, Legallic S, et al. Mutation of the PDGFRB gene as a cause of idiopathic basal ganglia calcification. *Neurology.* 2013;80(2):181–7. <https://doi.org/10.1212/WNL.0b013e31827ccf34>
 19. Keller A, Westenberger A, Sobrido MJ, García-Murias M, Domingo A, Sears RL, et al. Mutations in the gene encoding PDGF-B cause brain calcifications in humans and mice. *Nat Genet.* 2013;45(9):1077–82. <https://doi.org/10.1038/ng.2723>
 20. Yao XP, Cheng X, Wang C, Zhao M, Guo XX, Su HZ, et al. Biallelic mutations in MYORG cause autosomal recessive primary familial brain calcification. *Neuron.* 2018;98(6):1116–23. <https://doi.org/10.1016/j.neuron.2018.05.037>
 21. Schottlaender LV, Abeti R, Jaunmuktane Z, Wilson MS, Jurici S, Ayrignac X, et al. Bi-allelic JAM2 variants lead to early-onset recessive primary familial brain calcification. *Am J Hum Genet.* 2020;106(3):412–21. <https://doi.org/10.1016/j.ajhg.2020.02.007>
 22. Anheim M, Lopez-Sanchez U, Giovannini D, Richard AC, Touhami J, N'Guyen L, et al. XPR1 mutations are a rare cause of primary familial brain calcification. *J Neurol.* 2016;263(8):1559–64. <https://doi.org/10.1007/s00415-016-8166-4>
 23. Yao XP, Zhao M, Wang C, Guo XX, Su HZ, Dong EL, et al. Analysis of gene expression and functional characterization of XPR1: a pathogenic gene for primary familial brain calcification. *Cell Tissue Res.* 2017;370(2):267–73. <https://doi.org/10.1007/s00441-017-2663-3>
 24. Guo XX, Zou XH, Wang C, Yao XP, Su HZ, Lai LL, et al. Spectrum of SLC20A2, PDGFRB, PDGFB, and XPR1 mutations in a large cohort of patients with primary familial brain calcification. *Hum Mutat.* 2019;40(4):392–403. <https://doi.org/10.1002/humu.23703>
 25. Gomez CR, Luque A, Horenstein S. Microvasculopathy may precede idiopathic cerebral calcifications—case report. *Angiology.* 1989;40(1):67–72. <https://doi.org/10.1177/000331978904000113>
 26. Miklossy J, Mackenzie IR, Dorovini-Zis K, Calne DB, Wszolek ZK, Klegeris A, et al. Severe vascular disturbance in a case of familial brain calcinosis. *Acta Neuropathol.* 2005;109(6):643–53. <https://doi.org/10.1007/s00401-005-1007-7>
 27. Wider C, Dickson DW, Schweitzer KJ, Broderick DF, Wszolek ZK. Familial idiopathic basal ganglia calcification: a challenging clinical-pathological correlation. *J Neurol.* 2009;256(5):839–42. <https://doi.org/10.1007/s00415-009-5025-6>
 28. Kozik M, Kulczycki J. Laser-spectrographic analysis of the cation content in Fahr's syndrome. *Arch Psychiatr Nervenkr.* 1978;225(2):135–42. <https://doi.org/10.1007/BF00343397>
 29. Kimura T, Miura T, Aoki K, Saito S, Hondo H, Konno T, et al. Familial idiopathic basal ganglia calcification: histopathologic features of an autopsied patient with an SLC20A2 mutation. *Neuropathology.* 2016;36(4):365–71. <https://doi.org/10.1111/neup.12280>
 30. Koyama S, Sato H, Kobayashi R, Kawakatsu S, Kurimura M, Wada M, et al. Clinical and radiological diversity in genetically confirmed primary familial brain calcification. *Sci Rep.* 2017;7(1):12046. <https://doi.org/10.1038/s41598-017-11595-1>
 31. Saito T, Nakamura M, Shimizu T, Oda K, Ishiwata K, Ishii K, et al. Neuroradiologic evidence of pre-synaptic and post-synaptic nigrostriatal dopaminergic dysfunction in idiopathic basal ganglia calcification: a case report. *J Neuroimaging.* 2010;20(2):189–91. <https://doi.org/10.1111/j.1552-6569.2008.00314.x>
 32. Jensen N, Schroder HD, Hejbol EK, Fuchtbauer EM, de Oliveira JR, Pedersen L. Loss of function of Slc20a2 associated with familial idiopathic basal ganglia calcification in humans causes brain calcifications in mice. *J Mol Neurosci.* 2013;51(3):994–9. <https://doi.org/10.1007/s12031-013-0085-6>
 33. Wallingford MC, Chia JJ, Leaf EM, Borgeia S, Chavkin NW, Sawangmake C, et al. SLC20A2 deficiency in mice leads to elevated phosphate levels in cerebrospinal fluid and glymphatic pathway-associated arteriolar calcification, and recapitulates human idiopathic basal ganglia calcification. *Brain Pathol.* 2017;27(1):64–76. <https://doi.org/10.1111/bpa.12362>
 34. Ansermet C, Moor MB, Centeno G, Auberson M, Hu DZ, Baron R, et al. Renal Fanconi syndrome and hypophosphatemic rickets in the absence of xenotropic and polytropic retroviral receptor in the nephron. *J Am Soc Nephrol.* 2017;28(4):1073–8. <https://doi.org/10.1681/ASN.2016070726>
 35. Xu X, Li X, Sun H, Cao Z, Gao R, Niu T, et al. Murine placental-fetal phosphate dyshomeostasis caused by an Xpr1 deficiency accelerates placental calcification and restricts fetal growth in late gestation. *J Bone Miner Res.* 2020;35(1):116–29. <https://doi.org/10.1002/jbmr.3866>
 36. Skarnes WC, Rosen B, West AP, et al. A conditional knockout resource for the genome-wide study of mouse gene function. *Nature.* 2011;474(7351):337–42. <https://doi.org/10.1038/nature10163>
 37. Renier N, Wu Z, Simon DJ, Yang J, Ariel P, Tessier-Lavigne M. iDISCO: a simple, rapid method to immunolabel large tissue samples for volume imaging. *Cell.* 2014;159(4):896–910. <https://doi.org/10.1016/j.cell.2014.10.010>
 38. Voigt FF, Kirschenbaum D, Platonova E, Pagès S, Campbell RAA, Kastli R, et al. The mesoSPIM initiative: open-source light-sheet microscopes for imaging cleared tissue. *Nat Methods.* 2019;16(11):1105–8. <https://doi.org/10.1038/s41592-019-0554-0>
 39. Horstmann H, Körber C, Sätzler K, Aydin D, Kuner T. Serial section scanning electron microscopy (S3EM) on silicon wafers for ultra-structural volume imaging of cells and tissues. *PLoS One.* 2012;7(4):e35172. <https://doi.org/10.1371/journal.pone.0035172>

40. Franke T, Kolotuev I. Array tomography workflow for the targeted acquisition of volume information using scanning electron microscopy. *J Vis Exp*. 2021;(173). <https://doi.org/10.3791/61847>
41. Cardona A, Saalfeld S, Schindelin J, Arganda-Carreras I, Preibisch S, Longair M, et al. TrakEM2 software for neural circuit reconstruction. *PLoS One*. 2012;7(6):e38011. <https://doi.org/10.1371/journal.pone.0038011>
42. Schindelin J, Arganda-Carreras I, Frise E, et al. Fiji: an open-source platform for biological-image analysis. *Nat Methods*. 2012; 9(7):676–82. <https://doi.org/10.1038/nmeth.2019>
43. Zarb Y, Weber-Stadlbauer U, Kirschenbaum D, et al. Ossified blood vessels in primary familial brain calcification elicit a neurotoxic astrocyte response. *Brain*. 2019;142(4):885–902. <https://doi.org/10.1093/brain/awz032>
44. Jensen N, Schroder HD, Hejbol EK, et al. Mice knocked out for the primary brain calcification-associated gene *Slc20a2* show unimpaired prenatal survival but retarded growth and nodules in the brain that grow and calcify over time. *Am J Pathol*. 2018; 188(8):1865–81. <https://doi.org/10.1016/j.ajpath.2018.04.010>
45. Fraser H. Bilateral thalamic calcification in ageing mice. *J Pathol Bacteriol*. 1968;96(1):220–2. <https://doi.org/10.1002/path.1700960124>
46. Fraser H, Dickinson AG. The sequential development of the brain lesion of scrapie in three strains of mice. *J Comp Pathol*. 1968; 78(3):301–11. [https://doi.org/10.1016/0021-9975\(68\)90006-6](https://doi.org/10.1016/0021-9975(68)90006-6)
47. Morgan KT, Johnson BP, Frith CH, Townsend J. An ultrastructural study of spontaneous mineralization in the brains of aging mice. *Acta Neuropathol*. 1982;58(2):120–4. <https://doi.org/10.1007/BF00691652>
48. Huang YT, Zhang LH, Li MF, Cheng L, Qu J, Cheng Y, et al. Clinical features of primary familial brain calcification in 17 families. *Chin Med J (Engl)*. 2018;131(24):2997–3000. <https://doi.org/10.4103/0366-6999.247218>
49. Zarb Y, Sridhar S, Nassiri S, Utz SG, Schaffnerath J, Maheshwari U, et al. Microglia control small vessel calcification via TREM2. *Sci Adv*. 2021;7(9):eabc4898. <https://doi.org/10.1126/sciadv.abc4898>
50. Nahar K, Lebouvier T, Andaloussi Mae M, Konzer A, Bergquist J, Zarb Y, et al. Astrocyte-microglial association and matrix composition are common events in the natural history of primary familial brain calcification. *Brain Pathol*. 2020;30(3):446–64. <https://doi.org/10.1111/bpa.12787>
51. Sherriff FE, Bridges LR, Gentleman SM, Sivaloganathan S, Wilson S. Markers of axonal injury in post mortem human brain. *Acta Neuropathol*. 1994;88(5):433–9. <https://doi.org/10.1007/BF00389495>
52. Hannocks MJ, Pizzo ME, Huppert J, Deshpande T, Abbott NJ, Thorne RG, et al. Molecular characterization of perivascular drainage pathways in the murine brain. *J Cereb Blood Flow Metab*. 2018;38(4):669–86. <https://doi.org/10.1177/0271678X17749689>
53. Lee MY, Choi JS, Lim SW, Cha JH, Chun MH, Chung JW. Expression of osteopontin mRNA in developing rat brainstem and cerebellum. *Cell Tissue Res*. 2001;306(2):179–85. <https://doi.org/10.1007/s004410100456>
54. Hubbard AK, Rothlein R. Intercellular adhesion molecule-1 (ICAM-1) expression and cell signaling cascades. *Free Radic Biol Med*. 2000;28(9):1379–86. [https://doi.org/10.1016/s0891-5849\(00\)00223-9](https://doi.org/10.1016/s0891-5849(00)00223-9)
55. Bisht K, Sharma KP, Lecours C, Gabriela Sánchez M, el Hajj H, Milior G, et al. Dark microglia: a new phenotype predominantly associated with pathological states. *Glia*. 2016;64(5):826–39. <https://doi.org/10.1002/glia.22966>
56. Gajardo-Gomez R, Labra VC, Orellana JA. Connexins and pannexins: new insights into microglial functions and dysfunctions. *Front Mol Neurosci*. 2016;9:86. <https://doi.org/10.3389/fnmol.2016.00086>
57. Hoffman HS, Searle JL. Acoustic variables in the modification of startle reaction in the rat. *J Comp Physiol Psychol*. 1965;60:53–8. <https://doi.org/10.1037/h0022325>
58. Kim KM. Apoptosis and calcification. *Scanning Microsc*. 1995; 9(4):1137–75. discussion 1175–8.
59. Voelkl J, Lang F, Eckardt KU, Amann K, Kuro-o M, Pasch A, et al. Signaling pathways involved in vascular smooth muscle cell calcification during hyperphosphatemia. *Cell Mol Life Sci*. 2019; 76(11):2077–91. <https://doi.org/10.1007/s00018-019-03054-z>
60. Hozumi I, Kurita H, Ozawa K, Furuta N, Inden M, Sekine SI, et al. Inorganic phosphorus (Pi) in CSF is a biomarker for SLC20A2-associated idiopathic basal ganglia calcification (IBGC1). *J Neurol Sci*. 2018;388:150–4. <https://doi.org/10.1016/j.jns.2018.03.014>
61. Nicolas G, Marguet F, Laquerriere A, Mendes de Oliveira JR, Hannequin D. Microangiopathy in primary familial brain calcification: evidence from skin biopsies. *Neurol Genet*. 2017;3(2):e134. <https://doi.org/10.1212/NXG.000000000000134>
62. Biancheri R, Severino M, Robbiano A, Iacomino M, Del Sette M, Minetti C, et al. White matter involvement in a family with a novel PDGFB mutation. *Neurol Genet*. 2016;2(3):e77. <https://doi.org/10.1212/NXG.000000000000077>
63. Sakai K, Ishida C, Hayashi K, Tsuji N, Kannon T, Hosomichi K, et al. Familial idiopathic basal ganglia calcification with a heterozygous missense variant (c.902C>T/p.P307L) in SLC20A2 showing widespread cerebrovascular lesions. *Neuropathology*. 2022; 42(2):126–33. <https://doi.org/10.1111/neup.12781>
64. Zhang X, Ma G, Zhao Z, Zhu M. SCL20A2 mutation presenting with acute ischemic stroke: a case report. *BMC Neurol*. 2018; 18(1):11. <https://doi.org/10.1186/s12883-018-1012-9>
65. Gao L, Chen J, Dong H, Li X. A novel mutation in MYORG leads to primary familial brain calcification and cerebral infarction. *Int J Neurosci*. 2022;132(12):1182–6. <https://doi.org/10.1080/00207454.2020.1869000>
66. Magistrelli L, Croce R, De Marchi F, et al. Expanding the genetic spectrum of primary familial brain calcification due to SLC20A2 mutations: a case series. *Neurogenetics*. 2021;22(1):65–70. <https://doi.org/10.1007/s10048-021-00634-9>
67. Uygur GA, Liu Y, Hellman RS, Tikofsky RS, Collier BD. Evaluation of regional cerebral blood flow in massive intracerebral calcifications. *J Nucl Med*. 1995;36(4):610–2.
68. Borges-Medeiros RL, Ferreira LD, de Oliveira JRM. Lack of major ophthalmic findings in patients with primary familial brain calcification linked to SLC20A2 and PDGFB. *J Mol Neurosci*. 2019;67(3):441–4. <https://doi.org/10.1007/s12031-018-1250-8>
69. Hosli L, Binini N, Ferrari KD, et al. Decoupling astrocytes in adult mice impairs synaptic plasticity and spatial learning. *Cell Rep*. 2022;38(10):110484. <https://doi.org/10.1016/j.celrep.2022.110484>
70. Salman MM, Kitchen P, Halsey A, Wang MX, Törnroth-Horsefield S, Conner AC, et al. Emerging roles for dynamic aquaporin-4 subcellular relocalization in CNS water homeostasis. *Brain*. 2022;145(1):64–75. <https://doi.org/10.1093/brain/awab311>
71. St-Pierre MK, Carrier M, Gonzalez Ibanez F, et al. Ultrastructural characterization of dark microglia during aging in a mouse model of Alzheimer's disease pathology and in human post-mortem brain samples. *J Neuroinflammation*. 2022;19(1):235. <https://doi.org/10.1186/s12974-022-02595-8>
72. Sato H, Sato M. Ultrastructural morphology of thalamic cytoplasmic inclusion bodies in El mouse. *Exp Neurol*. 1986;93(1):160–7. [https://doi.org/10.1016/0014-4886\(86\)90155-x](https://doi.org/10.1016/0014-4886(86)90155-x)
73. Yanai T, Masegi T, Yoshida K, Ishikawa K, Kawada M, Iwasaki T, et al. Eosinophilic neuronal inclusions in the thalamus of ageing B6C3F1 mice. *J Comp Pathol*. 1995;113(3):287–90. [https://doi.org/10.1016/s0021-9975\(05\)80043-x](https://doi.org/10.1016/s0021-9975(05)80043-x)
74. Maetzler W, Berg D, Funke C, Sandmann F, Stünitz H, Maetzler C, et al. Progressive secondary neurodegeneration and microcalcification co-occur in osteopontin-deficient mice. *Am J*

- Pathol. 2010;177(2):829–39. <https://doi.org/10.2353/ajpath.2010.090798>
75. Meireles AM, Shiao CE, Guenther CA, Sidik H, Kingsley DM, Talbot WS. The phosphate exporter *xpr1b* is required for differentiation of tissue-resident macrophages. *Cell Rep.* 2014;8(6):1659–67. <https://doi.org/10.1016/j.celrep.2014.08.018>
76. Ren Y, Shen Y, Si N, Fan S, Zhang Y, Xu W, et al. *Slc20a2*-deficient mice exhibit multisystem abnormalities and impaired spatial learning memory and sensorimotor gating but normal motor coordination abilities. *Front Genet.* 2021;12:639935. <https://doi.org/10.3389/fgene.2021.639935>
77. Morgan CA 3rd, Southwick SM, Grillon C, Davis M, Krystal JH, Charney DS. Yohimbine-facilitated acoustic startle reflex in humans. *Psychopharmacology (Berl).* 1993;110(3):342–6. <https://doi.org/10.1007/BF02251291>
78. Vaughan AE, Mendoza R, Aranda R, Battini JL, Miller AD. *Xpr1* is an atypical G-protein-coupled receptor that mediates xenotropic and polytropic murine retrovirus neurotoxicity. *J Virol.* 2012;86(3):1661–9. <https://doi.org/10.1128/JVI.06073-11>
79. Nicolas G, Charbonnier C, de Lemos RR, Richard AC, Guillin O, Wallon D, et al. Brain calcification process and phenotypes according to age and sex: Lessons from *SLC20A2*, *PDGFB*, and *PDGFRB* mutation carriers. *Am J Med Genet B* Neuropsychiatr Genet. 2015;168(7):586–94. <https://doi.org/10.1002/ajmg.b.32336>
80. Woodward HJ, Zhu D, Hadoke PWF, MacRae VE. Regulatory role of sex hormones in cardiovascular calcification. *Int J Mol Sci.* 2021;22(9):4620. <https://doi.org/10.3390/ijms22094620>

SUPPORTING INFORMATION

Additional supporting information can be found online in the Supporting Information section at the end of this article.

How to cite this article: Maheshwari U, Mateos JM, Weber-Stadlbauer U, Ni R, Tamatey V, Sridhar S, et al. Inorganic phosphate exporter heterozygosity in mice leads to brain vascular calcification, microangiopathy, and microgliosis. *Brain Pathology.* 2023;33(6):e13189. <https://doi.org/10.1111/bpa.13189>